

**COMPARISON OF MELTING LEVEL ALTITUDES FROM THE NCEP
REANALYSIS WITH TRMM PRECIPITATION RADAR DATA**

A Thesis

by

GETTYS NUNN HARRIS, JR.

Submitted to the Office of Graduate Studies of
Texas A&M University
in partial fulfillment of the requirements for the degree of

MASTER OF SCIENCE

August 1999

Major Subject: Meteorology

19990907 170

DISTRIBUTION STATEMENT A
Approved for Public Release
Distribution Unlimited

DTIC QUALITY INSPECTED 4

REPORT DOCUMENTATION PAGE

*Form Approved
OMB No. 0704-0188*

Public reporting burden for this collection of information is estimated to average 1 hour per response, including the time for reviewing instructions, searching existing data sources, gathering and maintaining the data needed, and completing and reviewing the collection of information. Send comments regarding this burden estimate or any other aspect of this collection of information, including suggestions for reducing this burden, to Washington Headquarters Services, Directorate for Information Operations and Reports, 1215 Jefferson Davis Highway, Suite 1204, Arlington, VA 22202-4302, and to the Office of Management and Budget, Paperwork Reduction Project (0704-0188), Washington, DC 20503.

1. AGENCY USE ONLY (Leave blank)		2. REPORT DATE 13.Aug.99	3. REPORT TYPE AND DATES COVERED THESIS	
4. TITLE AND SUBTITLE COMPARISON OF MELTING LEVEL ALTITUDES FROM THE NCEP REANALYSIS WITH TRMM PRECIPITATION RADAR DATA			5. FUNDING NUMBERS	
6. AUTHOR(S) CAPT HARRIS GETTYS N				
7. PERFORMING ORGANIZATION NAME(S) AND ADDRESS(ES) TEXAS A&M UNIVERSITY			8. PERFORMING ORGANIZATION REPORT NUMBER	
9. SPONSORING/MONITORING AGENCY NAME(S) AND ADDRESS(ES) THE DEPARTMENT OF THE AIR FORCE AFIT/CIA, BLDG 125 2950 P STREET WPAFB OH 45433			10. SPONSORING/MONITORING AGENCY REPORT NUMBER FY99-227	
11. SUPPLEMENTARY NOTES				
12a. DISTRIBUTION AVAILABILITY STATEMENT Unlimited distribution In Accordance With AFI 35-205/AFIT Sup 1			12b. DISTRIBUTION CODE	
13. ABSTRACT (Maximum 200 words)				
14. SUBJECT TERMS			15. NUMBER OF PAGES 60	
			16. PRICE CODE	
17. SECURITY CLASSIFICATION OF REPORT	18. SECURITY CLASSIFICATION OF THIS PAGE	19. SECURITY CLASSIFICATION OF ABSTRACT	20. LIMITATION OF ABSTRACT	

**COMPARISON OF MELTING LEVEL ALTITUDES FROM THE NCEP
REANALYSIS WITH TRMM PRECIPITATION RADAR DATA**

A Thesis

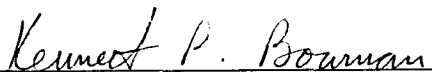
by

GETTYS NUNN HARRIS, JR.

Submitted to Texas A&M University
in partial fulfillment of the requirements
for the degree of

MASTER OF SCIENCE

Approved as to style and content by:


Kenneth P. Bowman
(Chair of Committee)


Gerald R. North
(Member)


Ping Chang
(Member)


Gerald R. North
(Head of Department)

August 1999

Major Subject: Meteorology

ABSTRACT

Comparison of Melting Level Altitudes from the NCEP Reanalysis
with TRMM Precipitation Radar Data. (August 1999)

Gettys Nunn Harris, Jr., B.S., North Carolina State University;

M.A., University of Oklahoma

Chair of Advisory Committee: Dr. Kenneth P. Bowman

Tropical Rainfall Measuring Mission Precipitation Radar (TRMM PR) reflectivity data is compared with freezing level (altitude of the 0° C isotherm) values derived from National Center for Environmental Prediction (NCEP) 40-Year Reanalysis to determine the relationship between the two sets of data. To establish a baseline for comparison, a climatology of NCEP freezing level data is produced. NCEP freezing level is derived using a reverse linear interpolation scheme applied to the temperature profile for each gridpoint. Global monthly means and measures of variability are calculated for the period 1979-1998, and a 20-year global climatology is presented. Zonal means are calculated from the monthly mean data for 1998 and the 1979-1998 climatology.

The NCEP freezing level is considered a proxy for the melting level, and is compared with derived TRMM PR melting level values. Some difference is expected, as some time is required for frozen precipitation to fall through freezing level, melt, and create a melting layer and "bright band" signature. To estimate the height of the melting level, an algorithm is used to isolate the maximum reflectivity altitude in the vertical reflectivity profile of mature tropical convection. The 1998 monthly mean melting level from the TRMM PR data are compared to the calculated NCEP monthly means and 20-

year freezing level climatology. Generally, the TRMM PR retrieved values are about 600 m lower than the NCEP freezing level height and show similar spatial distribution to the NCEP data.

This work is dedicated to my wife, Jacquelynn, who with patience and understanding has supported my efforts to complete the requirements for this master's degree; I most certainly could not have done this without her. It is dedicated to my two children, Hayley and Gray, whom I hope will learn something from my striving for and reaching this goal. Mostly, I hope I have shown them the importance of persistence, learning, and not being afraid to try something that you feel might be beyond your grasp. Finally, I dedicate this work to my mother and father, Lois and Gettys N. Harris, Sr. They encouraged me to try hard, do my best, to not take myself – or life – too seriously, and after that just let things take care of themselves. It's good advice.

ACKNOWLEDGEMENTS

First and foremost, I thank Dr. Bowman for his guidance through this difficult process. His seemingly endless knowledge of programming and insights into solving problems saved me from myself many times, and eventually I started to get an idea of what science is all about. Dr. Bowman's calm demeanor made life easier for those of us who may have had "panic attacks" over getting done on time; he maintained (at least outwardly) the confidence I could finish on time and had a plan to help me do so. For all of his help and involvement, I am grateful. I also thank committee members Drs. Jerry North and Ping Chang for their thoughts and comments, which helped not only in the preparation of this thesis but in the execution of my research. Their experienced criticism and encouragement was indispensable.

I must place a special acknowledgement here for the good friends I made since coming here. Certainly, I would not have been able to complete my research without their inputs, assistance, and friendship. First, I must recognize Mr. Dong-Bin Shin, whose work provided the comparison data set for this thesis. I thank him also for his advice on my research proposal, computer programs he gave me, and his eagerness to answer questions about his (our) research. Capt Rick Wagner's detailed computer programs made up the basis of many of my own programs. Rick's help during the hopeless hours in room 1010 cranking on dynamics and physics also requires many thanks. Lt/Capt Neil Sanger's enthusiasm and optimism changed my attitude on many days. His dedication to his faith, work, and physical fitness kept me on course in those aspects of my own life. Capt Kyle Bellue's even temper and sense of humor helped me maintain my own. Frank Leahy helped me and others solve problems in dynamics and physics that we felt we'd never get solved. His hackey-sack provided hours of much

needed relief from our mind-bending tasks, and who can forget fantasy football and “the beatings?”

Chris Bellows helped me survive METR 655 (Satellite) and helped me think through and solidify a few concepts in this thesis. He’s been a good friend with whom to work out, shoot the bull, or to take a break and get coffee over at the Pavilion. Michele Nordeen and I commiserated often over IDL programming problems; I hope I gave her half as many solutions as she gave me. Dong Heon Lee not only helped me with dynamics, physics and satellite courses through that first semester, he patiently discussed with me things Korean. To each of you, and to any others who have helped, guided, advised, or motivated me, thanks. Last, but certainly not least, I promised my daughter Hayley that I would put some things that she learned in first-grade science class into my thesis. First, the sun is a star. Second, there is no air in space. Third, thunder comes from the clouds bumping together and making lightning. Thanks, Hayley.

TABLE OF CONTENTS

CHAPTER	Page
I INTRODUCTION AND BACKGROUND	1
1.1 Introduction	1
1.2 Microwave Rainfall Retrievals.....	3
1.3 Previous Studies	4
1.4 Objectives.....	6
II DATA AND METHODS.....	8
2.1 Data.....	8
2.2 Methods.....	9
III RESULTS.....	13
3.1 NCEP Instantaneous Freezing Level	13
3.2 Monthly Means.....	15
3.3 Climatological Monthly Means.....	17
3.4 Intramonth Standard Deviation	24
3.5 Interannual Variability of Monthly Means	28
3.6 Cross-Sectional Plots of the 1979-1998 Zonal Mean	34
3.7 Freezing Level Anomalies for 1998	37
3.8 Comparison Part I: Difference Maps.....	43
3.9 Comparison Part II: Zonal Means Cross-Sections	49
IV SUMMARY AND CONCLUSIONS	54
4.1 General.....	54
4.2 Statistics and Climatology	55
4.3 Comparisons.....	56
REFERENCES.....	58
VITA	60

LIST OF FIGURES

FIGURE		Page
1	Instantaneous Z_0 field for 00Z 1 January and 1 July 1998.	14
2	Monthly mean \bar{Z}_0 field for January and July 1998.....	16
3	Climatological monthly mean $\langle \bar{Z}_0 \rangle$ field for 1979-1998.	18
4	Intramonth standard deviation s_0 for selected months in 1998.	25
5	Interannual standard deviation S_0 for selected months.	29
6	Zonal cross-sections of $\langle \bar{Z}_0 \rangle$ for each month.....	35
7	1998 anomalies maps for \bar{Z}_0	38
8	Monthly raw differences between \bar{H}_0 and \bar{Z}_0	44
9	1998 mean difference $[\bar{H}_0] - [\bar{Z}_0]$	50
10	Cross-sections of $[\langle \bar{Z}_0 \rangle]$, $[\bar{H}_0]$, and $[\bar{Z}_0]$ for each month.	52
11	Cross-sections of $[\bar{H}_0] - [\langle \bar{Z}_0 \rangle]$ for each month.	53

CHAPTER I

INTRODUCTION AND BACKGROUND

1.1. Introduction

Beginning in the 1980s, the National Aeronautics and Space Administration (NASA) and Japan's National Space Development Agency (NASDA) joined to create the Tropical Rainfall Measuring Mission (TRMM), an endeavor to gather information about tropical rainfall in conjunction with NASA's Mission to Planet Earth (MTPE). On a global scale, most rain falls in the tropics, where the associated latent heat release is a major force in driving the global atmospheric circulation. TRMM's goals are to improve the observation of tropical precipitation, especially over the oceans where data is sparsest, and to make quantitative estimates of the latent heat release. Physical and technological limitations require that the TRMM satellite be in low-Earth orbit. This means that the satellite will only view a given location approximately twice per day, and thus can only *sample* the precipitation field. Therefore, TRMM's primary product will be estimates of monthly-mean precipitation on a 600 x 600 km grid over the tropical oceans [Simpson *et al.*, 1988].

In order to test and verify climate simulations and forecasts, high-quality observations of precipitation and latent heat release are needed [Simpson *et al.*, 1988]. Toward that end, TRMM is designed to gather data in a novel way to create monthly climatologies of rainfall in the tropics. The TRMM orbit is inclined 35° relative to the poles with an altitude of 350 km; this orbital configuration limits TRMM coverage to between 35°N and 35°S. Because this orbit precesses with respect to the Sun, the

This thesis follows the style and format of *Journal of Geophysical Research*.

satellite samples the diurnal cycle in a period of about a month. The satellite's low altitude improves horizontal resolution. These factors ultimately improve the data gathered for the monthly climatology products. *Shin and North* [1987] determined that the TRMM satellite data should yield monthly rainfall estimates with an error on the order of 10 percent [*Simpson et al.*, 1988].

To obtain this level of accuracy, TRMM carries five instruments, two of which are important to this research: the TRMM Precipitation Radar (PR) and the TRMM Microwave Imager (TMI). *Kummerow et al.* [1998] describes the TRMM sensor package in detail. The idea behind much of the design of TRMM is that the sensors will work together to produce better estimates of physical parameters than a single sensor can produce by itself. For instance, more accurate estimations of the melting level, derived from the PR, can be used to improve the TMI rain retrievals [*Wilheit, 1986; Tesmer and Wilheit, 1998*].

Since TRMM microwave rainfall retrievals are one of the primary motivations for this research, the TMI and PR sensors warrant discussion. The TMI is a passive multichannel microwave radiometer, with four dual-polarization frequencies (10, 19, 37 and 85.5 GHz vertical (V) and horizontal (H)) and one single-polarization frequency (21 GHz (V)), for a total of nine channels operating over TMI's 760 km swath. The TMI instrument is similar to the Special Sensor Microwave/Imager (SSM/I) flown on the Defense Meteorological Satellite Program (DMSP) satellites. The differences are: the two 10 GHz channels; a consistent scan geometry (no alternating A/B scan strategy); and higher spatial resolution [*TRMM Science Data and Information System*, 1997].

The PR is a single-channel, active microwave instrument, operating at a frequency of 13.8 GHz and scanning every 0.6 s across the satellite ground track. It records the signal returned from the surface and from atmospheric precipitation targets

encountered in its 215 km swath. Its scan structure consists of 49 conical rays, with the nadir view at the 25th ray position. The normal resolution along each ray is 250 m [TRMM Satellite Data and Information System, 1997].

1.2. Microwave Rainfall Retrievals

TMI data are used with various algorithms to retrieve instantaneous or averaged rain rates. The retrieval algorithms generally require the altitude of the freezing as an input to the algorithm. Many retrieval algorithms derive rainfall from TMI brightness temperatures by combining physical and statistical methods, using radiative transfer models coupled with empirical environmental ensemble data [Wilheit *et al.*, 1977].

Due to the varying nature of precipitation regimes, radiative transfer models must use different approaches in different rain situations. For example, the higher frequencies (> 37 GHz) detect the depletion of upwelling surface radiation due to scattering by ice particles. A scattering-type regime often exists in heavy rain-producing convective clouds extending above the freezing level; hence, scattering-based retrievals are useful for detecting rainfall in convective systems with high ice content. High-frequency channels are also used over land, which has high emissivity and contaminates low-frequency retrievals [Wilheit 1986; Liu and Curry, 1998].

At lower frequencies, absorption-emission by raindrops predominates. Rainfall is estimated by measuring raindrop emission and determining brightness temperature via Kirchoff's law; brightness temperature is then used in retrieval algorithms to derive the rainfall rate. The key factor in the lower-frequency retrievals is the ocean surface, which has low microwave emissivity, and thus provides a uniform cold background for detecting the emission regime in the precipitation above. Algorithms for deriving

rainfall in light rain or stratiform regimes use the lower channels (< 37 GHz), which are more sensitive to raindrop emission [Wilheit 1986; Liu and Curry, 1998].

For example, Chiu *et al.* [1990], following Wilheit *et al.* [1977], use a relatively simple relationship to determine rainfall. Their retrieval formula calculates rainrate as

$$T_b(R) = A - Be^{-C(z)R} \quad (1.1)$$

where T_b is the brightness temperature, R is rainfall rate, A is the background temperature (temperature of the underlying ocean surface), B is the dynamic range of the temperature variation, and C is a quadratic function of freezing level height.

Because the freezing level height affects the value for both B and C , the brightness temperature-rainfall rate relationship is sensitive to the freezing level value. In essence, a higher freezing level leads to higher rainfall rate, for rainfall rates up to 20 mm hr⁻¹.

Emission-based retrieval procedures, such as Shin *et al.* [1990] and Tesmer and Wilheit [1998], have similar sensitivity to the freezing level altitude. Although these algorithms take different approaches, each will improve as the accuracy of freezing level used in the algorithm increases. Shin *et al.* [1990] state that, "...if the freezing-level height can be estimated by multichannel information, the overall [retrieval] improvement will be enhanced." Tesmer and Wilheit [1998] agree: "TRMM algorithm development must take advantage of the information gained from the radar data, such as the height of the freezing level, and apply it over the remaining two-thirds of the TRMM [TMI] swath."

1.3. Previous Studies

Radar meteorologists use the term "melting layer" to describe the region (up to several hundred meters thick) just below the 0° C isotherm where the bright band appears. Conversely, much of the microwave rainfall retrieval research uses the familiar

aviation term “freezing level” for the location of the 0° C isotherm. To avoid confusion, this study will denote the NCEP freezing level – the altitude of the 0° C isotherm – with the symbol Z_0 , while the bright band or melting level altitude will be referred to as H_0 .

According to *Houze* [1997], the bright band occurs exclusively in stratiform-type precipitation: “...it is an unambiguous indicator of the presence of stratiform precipitation,” and is often found in areas containing convective cells. Frozen hydrometeors falling through the melting level create the bright band feature in PR data. Above Z_0 , frozen particles aggregate and become large enough to fall below the freezing level. When the aggregated ice particles reach above-freezing temperatures, melting begins. Since melting does not occur instantaneously, due to the snowflake aggregates melting from the outside in [*Austin and Bemis*, 1950; *Leary and Houze*, 1979], some time is required for the aggregate particles to melt completely.

While the ice particles melt, fall speed increases as they become more spherical. They finally overcome weaker, mature-stage updrafts – in tropical convection, 1-2 ms^{-1} [*Zipser and LeMone*, 1980] – and fall out. This creates a relatively narrow layer that contains large, water-covered ice particles that remain as the faster-moving raindrops fall from the layer. Reflectivity of the large, “wet” ice particles is ~7 dB higher than frozen hydrometeors above Z_0 , due mainly to an index of refraction 5 times greater and the increased particle dimension [*Rinehart*, 1997; *Houze*, 1997]. Thus, it is these melting, water-covered ice particles that cause a well-defined bright-band signature in radar images. Changes in dielectric properties as the particles change phase is also cited as an additional factor in creating the bright band signature [*Willis and Heymsfield*, 1989; *Houze*, 1997].

As tropical convection matures, the precipitation becomes more stratiform in nature, the area of stratiform precipitation increases, and the bright band grows in

horizontal extent. Identification of H_0 in the PR data is an indirect measure – with some difference expected due to the melting time – of the altitude of Z_0 .

Though this study considers Z_0 as a proxy for H_0 , it is clear that they are not the same quantity. Other studies have addressed the difference in Z_0 and H_0 derived from radiosonde data. The altitude difference between H_0 and Z_0 has been shown to vary substantially, depending on atmospheric conditions and geographical location. For bright band and freezing level heights presented in *Austin and Bemis* [1950], the mean bright band altitude was 3.3 km, while the mean difference ($H_0 - Z_0$) was –300 m, as seen from their radar in Cambridge, Massachusetts. *Stewart et al.* [1984] found the bright band to be about 300 m lower than the freezing level in stratiform precipitation of a maritime-type system in California. More importantly for this research, *Leary and Houze* [1979] found a mean H_0 of 4.5 km, and a difference ranging from –500 m to –900 m, in five tropical thunderstorm cases during GATE. The difference between Z_0 and H_0 will be apparent in the comparison of the two parameters.

Identification and classification of H_0 in tropical stratiform precipitation in PR data is currently underway in a project by D.-B. Shin of the Department of Meteorology at Texas A&M University. Shin (personal communication, 1999) uses a simple algorithm, similar to *Leary and Houze* [1979], to estimate H_0 from the PR data. This method focuses on finding the altitude of the maximum reflectivity in the vertical reflectivity structure of mature tropical storms. This data can be compared easily with the NCEP Z_0 data.

1.4. Objectives

The goal of this research is to determine the relationship between the altitudes melting levels retrieved from the TRMM PR and the NCEP analyzed freezing levels,

which are independent of the TRMM data. This will have a positive impact on future rainfall retrieval procedures. There are two parts to this main objective. First, a climatology of Z_0 derived from NCEP reanalysis is presented. The climatology shows the behavior of the global freezing level for 20 years beginning in January 1979. Within-month and climatological means and measures of variability are computed for each month, as are the 1998 Z_0 anomalies.

Second, because TRMM data has only been available since late 1997 (there is no H_0 climatology data), retrievals of the 1998 PR mean H_0 are directly compared to 1998 mean Z_0 values. Raw difference maps of mean H_0 and mean Z_0 are calculated and differences are presented for each month of 1998, and the yearly mean difference is shown. A comparison of monthly zonal means is presented; the zonal mean of the 1998 radar data is compared to the climatological mean data and the 1998 NCEP data. Finally, a zonal mean difference shows the behavior of the differences at different latitudes in the tropics. These comparisons reveal the similarity in distribution, and clearly defines the difference in magnitude, of the mean H_0 and Z_0 fields.

CHAPTER II

DATA AND METHODS

2.1. Data

The 40-year reanalysis by the National Centers for Environmental Prediction (NCEP) and National Center for Atmospheric Research (NCAR) is the data set used to calculate the freezing level climatology presented in this study. The reanalysis data are described in *Kalnay et al.* [1996]. The NCEP reanalysis contains data – primarily from radiosondes – which are augmented with satellite and other remote sensing data to compensate for lack of radiosonde data in some areas. Reanalysis data are archived every 6 hours on a 144 x 73 (2.5° x 2.5°) longitude-latitude grid, with 17 pressure levels in the vertical. An assimilation scheme, involving the insertion of observational data into a global forecast model, is used to produce the reanalysis. Most importantly, even though satellite data are incorporated into the reanalysis, TRMM data have not been used in constructing the NCEP data set. Therefore, the NCEP data and Shin's retrievals can be considered independent measures of the melting level.

Z_0 is determined from the NCEP reanalysis by reverse interpolation of the gridded vertical temperature profile at each horizontal grid point to find the geopotential height of the 0° C isotherm. Since NCEP temperature and geopotential height, according to *Kalnay et al.* [1996], are both "A" variables (most influenced by observations), and therefore the most reliable type, there is a high confidence in the interpolated values for Z_0 .

The H_0 dataset consists of values retrieved from TSDIS Level 1 PR reflectivity data. TSDIS uses the term level to designate the amount of processing done on the data; the least processed reflectivity data is the Level 1 data. To determine H_0 , the

retrieval algorithm uses only the nadir ray from each scan. This strategy was chosen for two reasons: 1) the nadir ray looks straight down on precipitation targets, eliminating angled views through the sides of storms; and 2) the availability of the “mirror” reflectivity image in the nadir data, which can be used to locate or verify the bright band. Nadir views at and above 1.5 km from each scan are used to calculate the height of H_0 . Then H_0 data is averaged over a $10^\circ \times 10^\circ$ box for a given month, thus creating the $\overline{H_0}$ dataset for the TRMM sensing area (35°S to 35°N).

2.2. Methods

2.2.1. NCEP Freezing Level Data

The altitude of the 0°C isotherm, symbolized by Z_0 , is derived from the NCEP reanalysis at 6-hour intervals by reverse interpolation of the temperature T as a function of geopotential height Z . The algorithm first searches each grid point’s vertical profile for levels where T first changes sign. The reverse linear interpolation scheme is applied to the two selected levels at the top and bottom of the layer. The algorithm checks for the occurrence of positive to negative temperature crossover only up to 200 mb (the 9th vertical pressure level). Truncating the vertical temperature profile allows computations to run faster by eliminating the upper half of the vertical profile, yet does not remove any possible occurrences of 0°C .

Additionally, there are two special cases to be considered: first, locations where $T < 0^\circ\text{C}$ throughout the entire profile; second, locations with multiple Z_0 ’s due to isothermal layers or inversions in the profile. In the case of no Z_0 (all temperatures at all levels are $< 0^\circ\text{C}$), the freezing level is considered to be missing and the gridpoint value is replaced by the IEEE Not-a-Number designation. In the case of more than one Z_0 being identified, the algorithm flags those locations, but stores only the lowest Z_0

value. Locations with multiple Z_0 occurrences account for less than 1 percent of the profiles overall, with no occurrences of multiple Z_0 's within 10° of the equator. The largest number of multiple Z_0 's is found in the high latitudes (around 60°) where multiple Z_0 's happen about 4 percent of the time.

The mean, variance, and standard deviation are calculated for each month. Intra-month monthly means ($\overline{Z_0}$) are calculated from the $\overline{Z_0}$ values from the NCEP data within each month. Intra-month variance (v_0) is calculated as the mean-squared deviation from the monthly mean, given by

$$Z_0' = Z_0 - \overline{Z_0}, \quad (4.1)$$

$$v_0 = \overline{Z_0'^2} \quad (4.2)$$

The intra-month standard deviation (s_0) is equal to $\sqrt{v_0}$.

Climatological monthly means and standard deviations are inter-annual values. Climatological monthly mean, $\langle \overline{Z_0} \rangle$ is the mean of the 20 monthly means for January, February, March, etc. The climatological variance and standard deviation represent the variability of the monthly mean about the climatological mean, given by

$$\overline{Z_0}' = \overline{Z_0} - \langle \overline{Z_0} \rangle, \quad (4.3)$$

$$V_0 = \langle \overline{Z_0}'^2 \rangle, \quad (4.4)$$

and $S_0 = \sqrt{V_0}$.

2.2.2. TRMM PR Data

In the comparison data set, estimates of H_0 are based on the position of the bright band (Shin, 1999, personal communication). Since stratiform and convective precipitation coexist in many tropical rainfall systems, retrievals of melting level height from PR data must recognize the difference between convective echoes and stratiform precipitation regions, because H_0 can only be unambiguously determined in stratiform

echoes, not convective cells. This does reduce the dataset appreciably; *Tokay and Short*, [1996] found precipitation area coverage measured by gages in the Tropical Ocean Global Atmosphere Couple Ocean-Atmosphere Experiment (TOGA-COARE) was composed of 74 percent stratiform and 26 percent convective rain, with total rainfall being 32 percent stratiform and 68 percent convective. *Cheng and Houze* [1979] found that stratiform precipitation in tropical convective systems accounts for around 40 percent of the total rainfall. *Houze* [1997] summarizes that "...a large component (~20 percent – 50 percent) of tropical precipitation exhibits stratiform radar echo structure."

Shin has accounted for the convective echoes from his data by applying an algorithm to vertical reflectivity profiles that selects only stratiform bright band regions as determined by specific criteria. His algorithm detects the melting level numerically. First, a single nadir reflectivity profile is drawn from the raw PR data. By using a data smoothing routine, the algorithm adjusts the vertical profile so that only major features remain; the reflectivity maximum (the bright band) is identified from these major features and is tested for validity.

Validity is determined by calculating the largest positive and negative gradients along the vertical profile for each scan element at every 250 m interval. The maximum gradient above the maximum-reflectivity point is determined, as is the minimum gradient of the profile below the maximum-reflectivity point. If these two values are within ± 1 km of the maximum reflectivity, the melting level is accepted; if not, the algorithm discards it. Thus, only mature-stage thunderstorms with well-defined bright bands are used to create the H_0 dataset. Convective cells and other cells not meeting the appropriate vertical structure criteria are ignored. The computed melting level data are binned into $10^\circ \times 10^\circ$ boxes over the TRMM sampling region and used to compute

monthly means $\overline{H_0}$. In order to compare the data more accurately, the NCEP $\overline{Z_0}$ data are re-binned from the original $2.5^\circ \times 2.5^\circ$ boxes to the $\overline{H_0}$ $10^\circ \times 10^\circ$ grid.

CHAPTER III

RESULTS

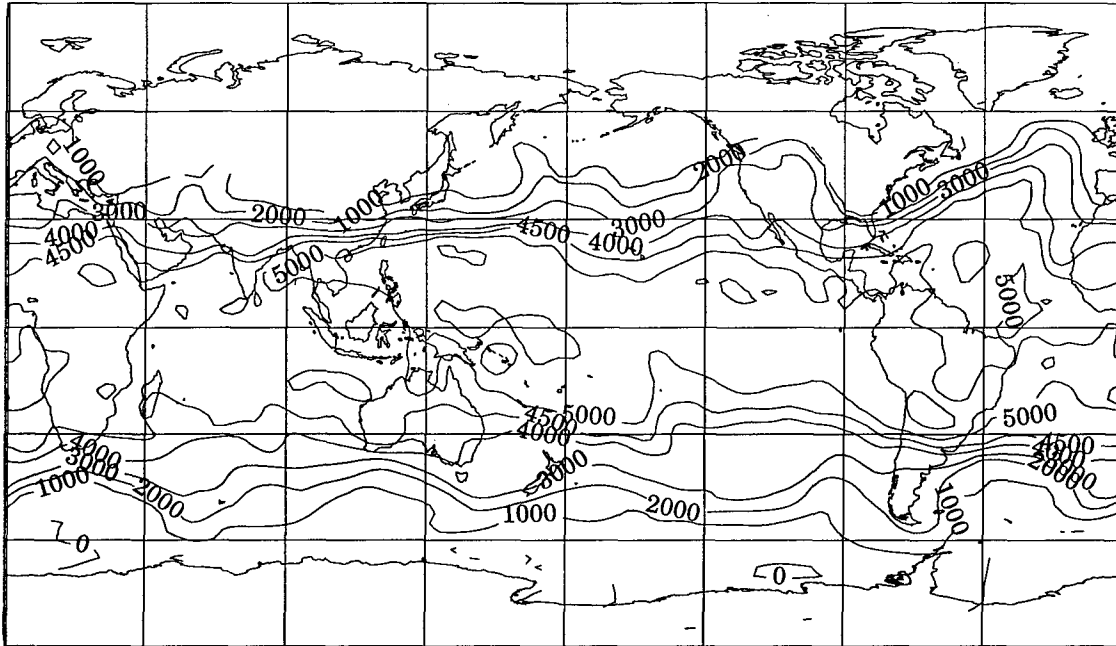
3.1. NCEP Instantaneous Freezing Level

Figure 1 shows an example of the instantaneous Z_0 field for 00Z, 1 January and July 1998. Regions with missing data ($T < 0^\circ \text{C}$ through the entire column) are not contoured. In January, for example, at 105°W the 1000 m contour reaches to $\sim 50^\circ\text{N}$, but is not continuous around the globe. Much of the continental area above 45°N has missing data. Contours are drawn at 0, 1000, 2000, 3000, 4000, 4500, 5000, 5500, and 6000 m on the Z_0 instantaneous maps.

In the rest of the NH, three regions are notable. First, there are strong gradients in Z_0 off the eastern NH continents where western boundary currents – the Kuroshio in the Pacific and the Gulf Stream in the Atlantic – carry warm water northward from the equator in close proximity to the cold continents. Away from the continents, the meridional gradients are weaker. In the tropics, from roughly 15°S to 15°N , the pattern is flat and roughly zonally symmetric. The exception to this is in the Atlantic, where the 5000 m contour extends north to almost 45°N . The SH pattern shows three areas of tight gradients, similar to those in the NH, off the Cape of Good Hope, E of New Zealand, and over southern South America and east into the central S Atlantic. Otherwise, the SH Z_0 gradient is loose and zonal, especially over the south central Pacific and Indian Oceans.

In July, only a few changes to the general pattern seen in January have taken place. Much more Z_0 data is available in the NH as summer solar insolation warms the continents. A strong closed 5500 m feature appears over India and the Himalayas in the summer monsoon. Also, the gradients in the SH tighten in the austral winter, especially over Australia and the Indian Ocean.

Z_0 (m) Date: 1998/ 1/ 1 Time: 00:00.00Z



Z_0 (m) Date: 1998/ 7/ 1 Time: 00:00.00Z

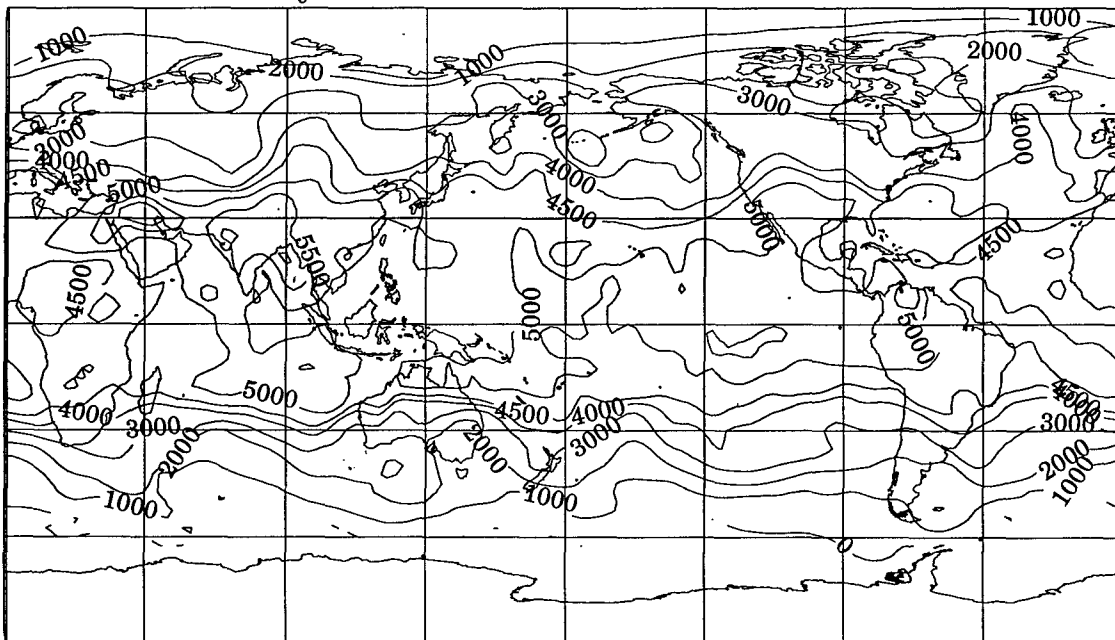


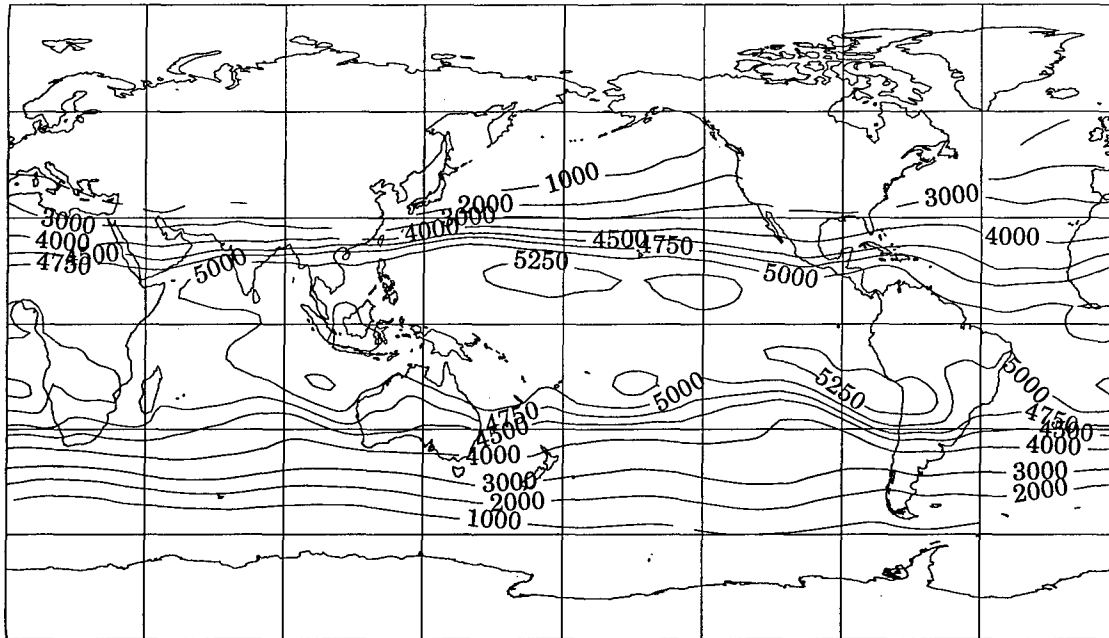
Figure 1. Instantaneous Z_0 field for 00Z 1 January and 1 July 1998. Contours are drawn at 0, 1000, 2000, 3000, 4000, 4500, 5000, 5500, and 6000 m.

3.2. Monthly Means

Figure 2 shows maps of monthly-mean freezing level height, \overline{Z}_0 , for two sample months, January and July 1998. Each monthly-mean map represents the mean of ~ 120 instantaneous Z_0 fields. As expected, the individual monthly means have a smoother pattern than the instantaneous plots in Figure 1. To show more detail in the tropics, where the Z_0 field is smooth, contours are drawn at 0, 1000, 2000, 3000, 4000, 4500, 4750, 5000, 5250, 5500, and 6000 m. The January map shows missing data, primarily over the continents, due to below-freezing temperatures through the column at some time during the month. Otherwise, there is an essentially zonal pattern associated with the freezing level. In the NH, the gradients are generally stronger from SW Asia to the western Pacific. Gradients are generally weaker from the eastern Pacific to the Atlantic. In the SH, a zonal pattern is apparent, with some small deviations over land, and generally weaker gradient. In and around the tropics, the \overline{Z}_0 field is flat and symmetric around the equator, with typical \overline{Z}_0 values of about 5000 m.

In July 1998, the zonal orientation and weak gradient of the \overline{Z}_0 field continue in the SH. In the NH, \overline{Z}_0 is generally lower over the oceans and higher over the continents, consistent with surface temperature variations. There is a prominent feature of high \overline{Z}_0 from the eastern Mediterranean Sea across the Indian subcontinent and Himalayas into SE Asia. In the NH, away from the Himalayas feature, the \overline{Z}_0 field shows weakening gradient through the tropics as higher heights bulge northward over NH continental areas. In the Pacific, another prominent feature shows up as a deep intrusion of lower heights into the low mid-latitudes west of Hawaii.

January 1998



July 1998

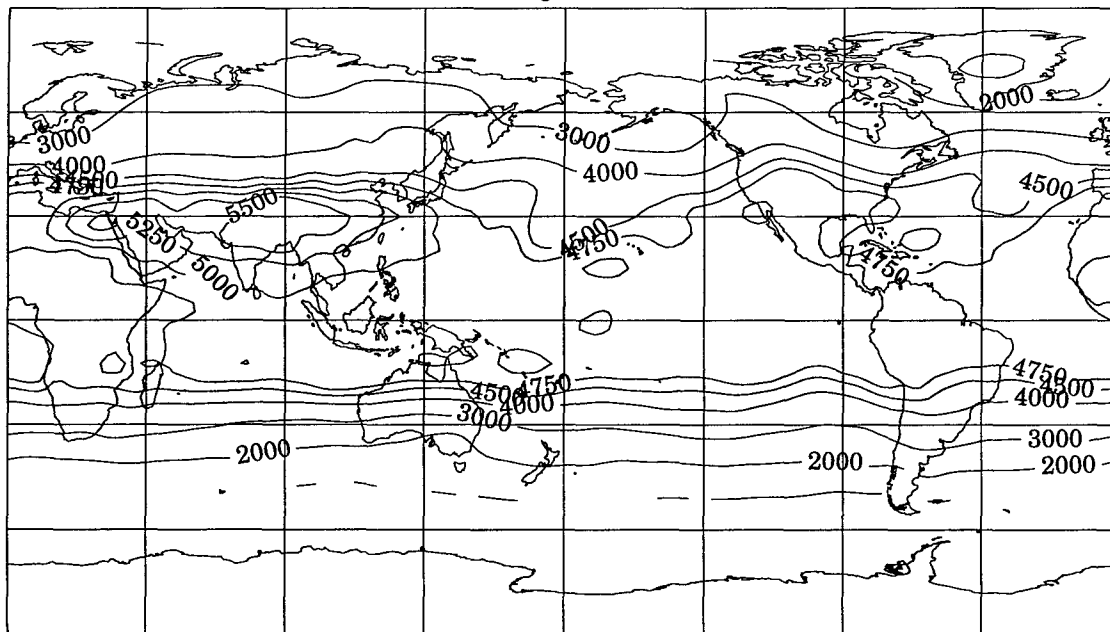


Figure 2. Monthly mean \bar{Z}_0 field for January and July 1998. Contours are drawn at 0, 1000, 2000, 3000, 4000, 4500, 4750, 5000, 5250, 5500, and 6000 m.

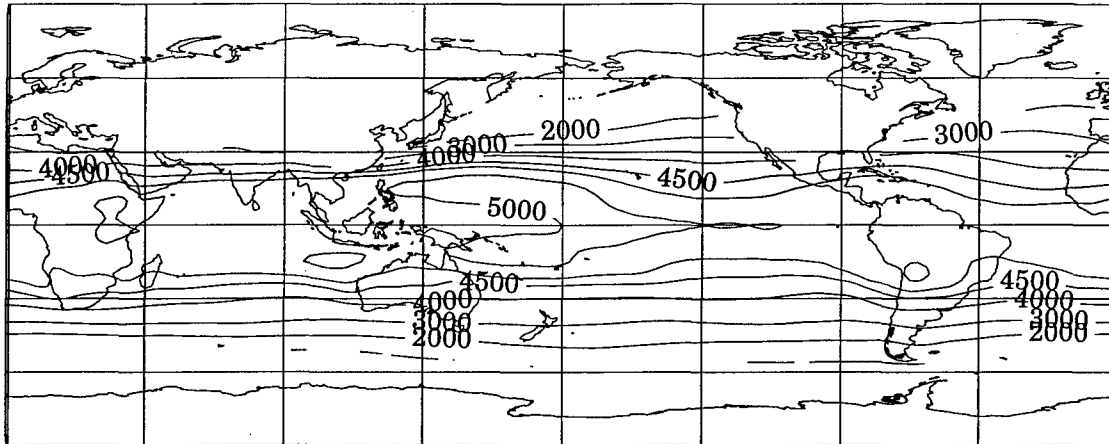
3.3. Climatological Monthly Means

Maps of climatological monthly means, $\langle \bar{Z}_0 \rangle$, for the 20-year period 1979-1998 are shown in Figure 3. As expected, these maps are smoother than the individual monthly mean maps in Figure 2. As in the monthly mean maps, the contours on the $\langle \bar{Z}_0 \rangle$ maps are drawn at 0, 1000, 2000, 3000, 4000, 4500, 4750, 5000, 5250, 5500, and 6000 m.

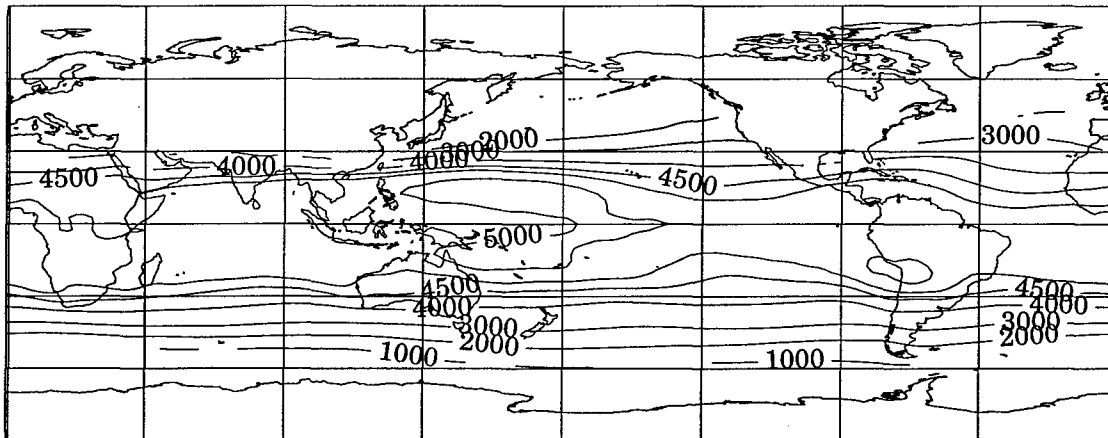
3.3.1. December-January-February. A prominent feature of Figure 3 is the large area of 5000 m enclosed in a dual-fingered shape centered on the equator in the central and western Pacific. An intrusion of lower heights centered on the equator from 125°E to 175°W divides the large area into two distinct regions around the equator which gradually weakens and moves east through the period. To the east of this feature, the 4750 m contours narrow toward the equator, reaching to 10° N and S at 90°W. In the Atlantic, north of the equator, $\langle \bar{Z}_0 \rangle$ is much lower than the values found in the tropics, with 3000 m values extending as far south as 20°N. The Indian Ocean maintains a flat symmetric pattern of Z_0 throughout the three-month period. Overall, away from the equatorial regions, the pattern is smooth and zonal, with some small deviations over land due to temperature differences (as expected) and missing data in the winter hemisphere.

A strong gradient is found off the coast of Asia, south of Japan in the western Pacific. This feature shows a strong decrease in contour values northward from the 5000 m values in the western equatorial Pacific to 2000 m at 30°N. This area of intense meridional gradient extends westward from from India into the central NH Pacific. Generally, strong gradients in the NH are seen over Asia, while the weakest gradients are found in the eastern and central Pacific and the tropical Atlantic.

December 1979-1998



January 1979-1998



February 1979-1998

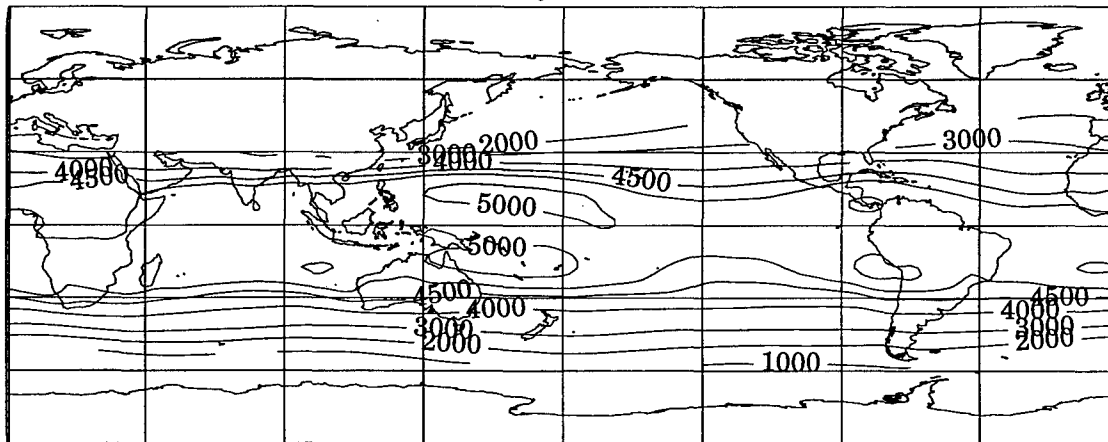
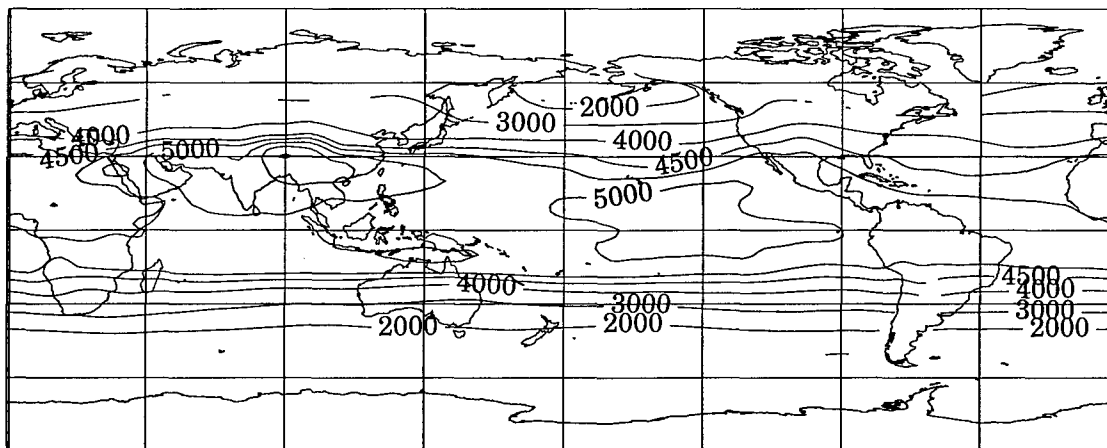
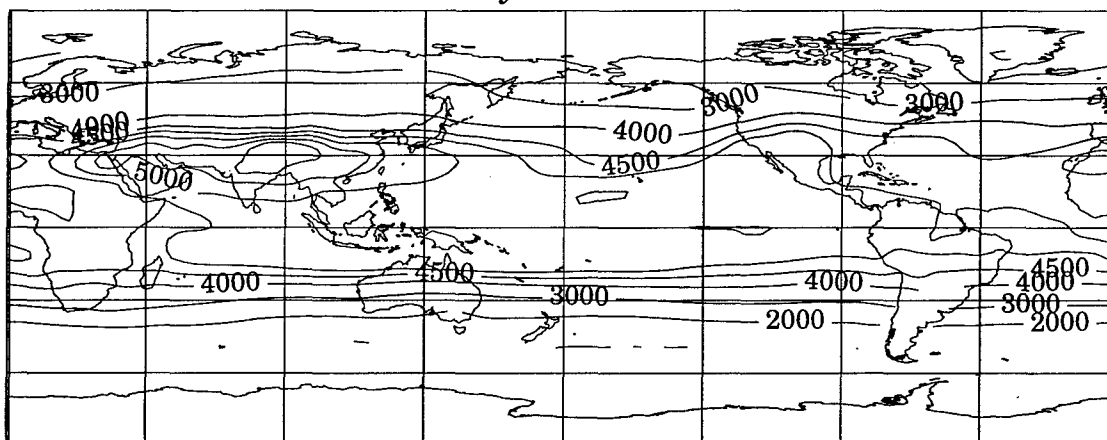


Figure 3. Climatological monthly mean $\langle \bar{Z}_0 \rangle$ field for 1979-1998. Contours are drawn at 0, 1000, 2000, 3000, 4000, 4500, 4750, 5000, 5250, 5500, and 6000 m.

June 1979-1998



July 1979-1998



August 1979-1998

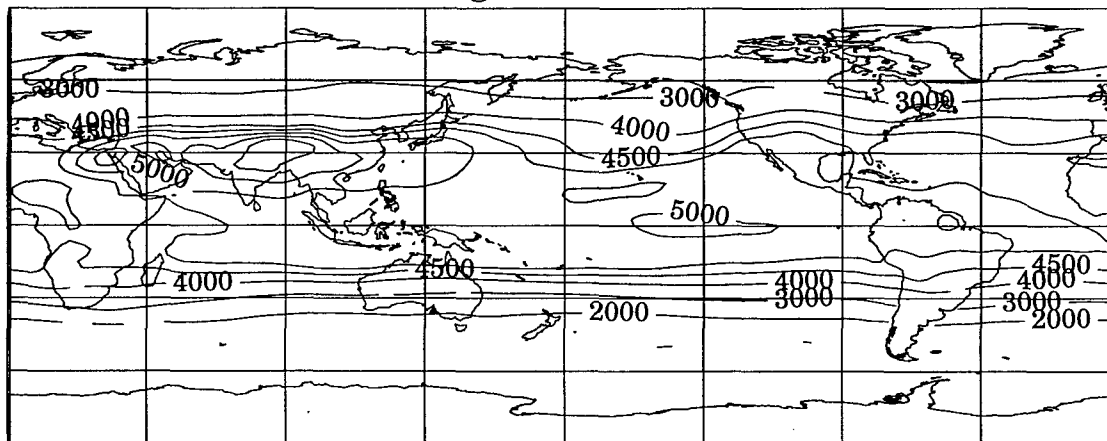
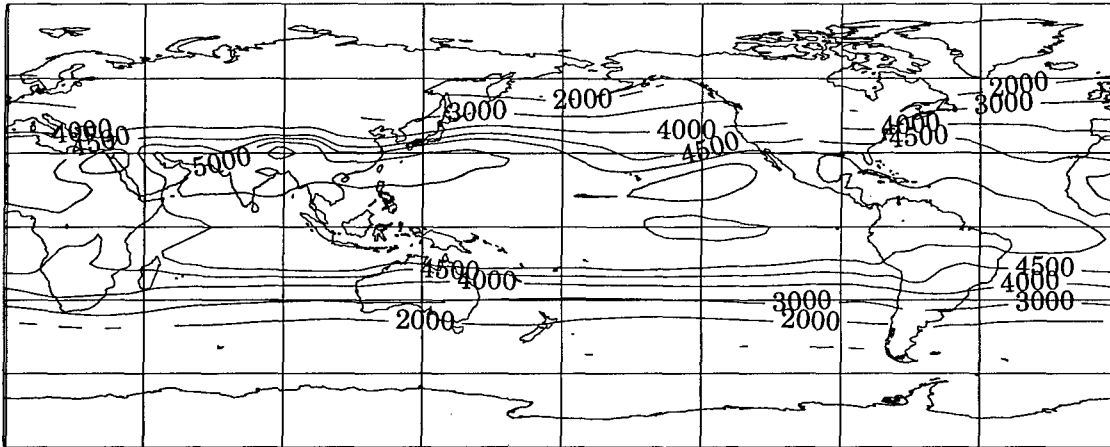
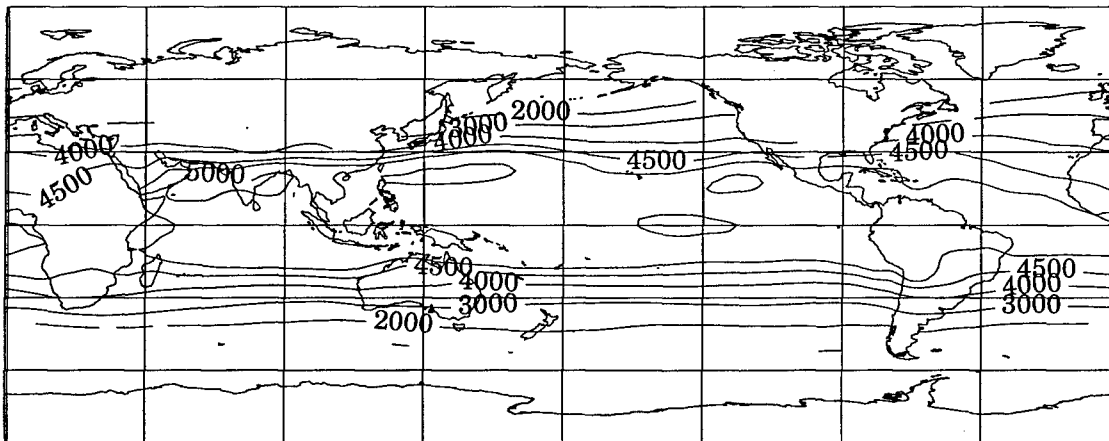


Figure 3. Continued.

September 1979-1998



October 1979-1998



November 1979-1998

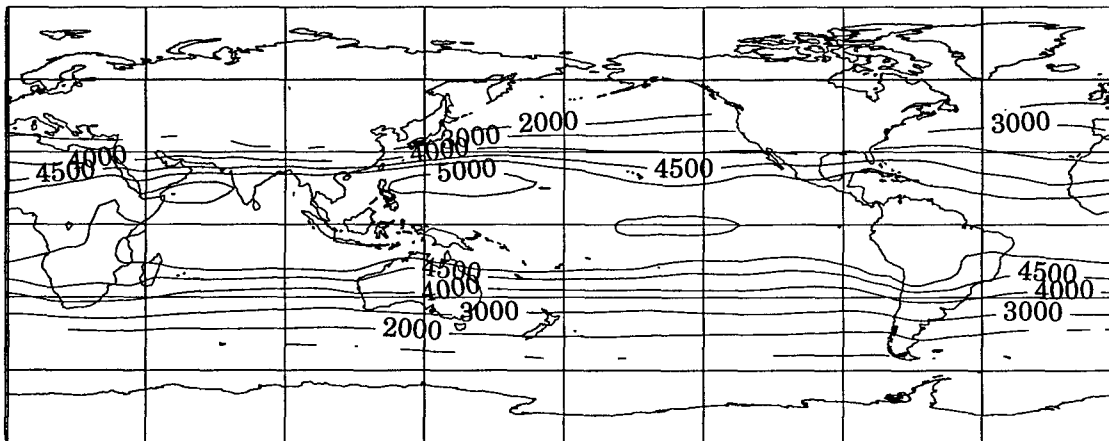


Figure 3. Continued.

Finally, the 1000 m field appears in the extreme south Pacific, off the coast of Antarctica at $\sim 60^{\circ}\text{S}$, 70°W , and maintains weak continuity around the continent. The gradient of $\langle \bar{Z}_0 \rangle$ in the Southern Hemisphere is much weaker than that in the Northern Hemisphere, and at 30°S and higher, the pattern is smooth and zonal, whereas the NH contours have much greater meridional fluctuation.

3.3.2. March-April-May. Broadening of the 5000 m contour in the Indian Ocean and western equatorial Pacific reverses a trend from the late winter, which showed this region to be shrinking. The 5000 m $\langle \bar{Z}_0 \rangle$ field is symmetrically-distributed around the equator and continues to grow zonally, with higher $\langle \bar{Z}_0 \rangle$ appearing in equatorial South America and expanding through the period. The equatorial 5000 m field reaches its greatest zonal extent in May. The SH remains largely zonal – the contours are almost straight lines – with weak gradients in the beginning of the season (fall in SH). However, the gradient strengthens as SH winter approaches; the 2000 m contour moves north about 10° while the 4750 m contour stays anchored at about 15°S .

In the NH, the field retains some meridional variability, with lower heights intruding south into the central Pacific and higher heights into North America. The gradient loosens in the NH overall, as evidenced by the disappearance of the strong winter gradient south of Japan and the movement of the 2000 m and 3000 m contours farther north over the western Pacific.

The eastward progression of the 5000 m field moves into the Indian Ocean from the Pacific, and the predominant wintertime $\langle \bar{Z}_0 \rangle$ values of 4750-5000 m around the equator gradually changes to > 5000 m by May; the northern portion of the 5000 m field over the Indian Ocean moves into the Bay of Bengal and Arabian Sea.

3.3.3. June-July-August. The high $\langle \bar{Z}_0 \rangle$ region over India and the Himalayas continues growing in the NH summer, with broad expansion of the region of 5000 m field from the > 5500 m center at 90°E , 30°N . In the Pacific, the 5000 m field gradually shrinks in zonal and meridional extent, disappearing completely in July and reappearing around the equator in the central Pacific in August. Interestingly, the entire $\langle \bar{Z}_0 \rangle$ field in the Indian Ocean shifts into the NH, obviously the effect of the summer monsoon. Much lower $\langle \bar{Z}_0 \rangle$ values are found in the SH tropical Indian Ocean as a result of this shift.

In the rest of the tropical regions, through the Pacific and Atlantic, the 4750 m field dominates. By the end of the season, a narrow corridor of 4500-4750 m values runs from west Africa at the equator into SE North America. In the mid-latitudes, even over the continents, the $\langle \bar{Z}_0 \rangle$ field maintains strong zonal pattern; a notable exception is the broad area of higher $\langle \bar{Z}_0 \rangle$ height over the Rocky Mountains in the United States. In the SH, the zonal pattern continues, but there is some indication that this pattern is changing, with some contour spreading in central South America.

3.3.4. September-October-November. A remnant of the large area of higher monsoon $\langle \bar{Z}_0 \rangle$ field over India and the Himalayas remains over India in September, but disappears in October, signaling the end of the monsoon. Over SE Asia and the western Pacific, reformation of the strong gradients begins as the growth of higher $\langle \bar{Z}_0 \rangle$ over the equatorial western Pacific begins again and cold air reappears over the continental areas, as evidenced by the preponderance of missing data.

Over the Atlantic, the corridor of 4500-4750 m $\langle \bar{Z}_0 \rangle$ heights narrows, eventually returning to its predominantly zonal orientation in November. The 4750 m field remains

the most common $\langle \bar{z}_0 \rangle$ value around the equator, both throughout the Pacific and Indian Oceans.

In the mid-latitudes, note the meridional fluctuations over SE Asia into the Pacific ocean. Generally, the pattern in the NH has gained more meridional orientation - especially over the Atlantic and eastern Pacific. The wavy NH pattern illustrates the difference between the NH and SH. In the SH - over the oceans especially - there are no comparable departures from zonal.

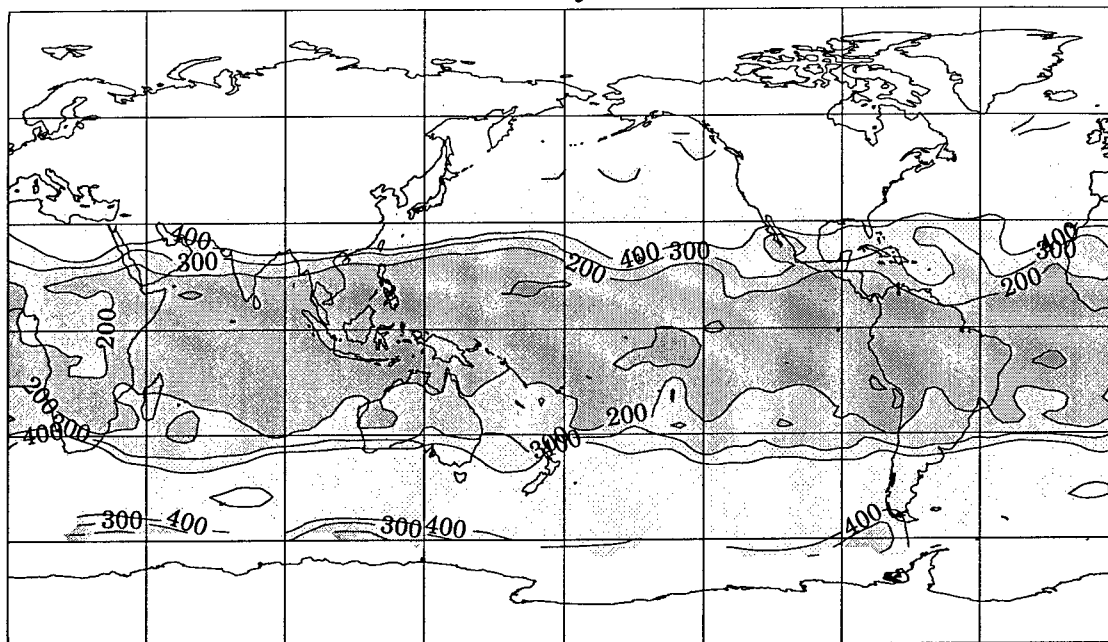
3.4. Intramonth Standard Deviation

3.4.1. January. The intramonth standard deviation s_0 is presented in Figure 4 for representative months from each season. Contours are drawn at 0, 25, 50, 75, 100, 200, 300, 400, and 500 m.

The January s_0 pattern shows zonally-oriented contours, increasing in value from a minimum near the equator to the maximum variability in the higher latitudes. Generally, the tropics - within about 15° of the equator - can be characterized by an s_0 of 200 m. January also shows the presence of cold air in the NH, with much of the data missing over the continents. Within the 200 m field, some small areas of lower variability occur, such as the 100 m contour at 170°W , 5°S . Additionally, there is a region of 300 m s_0 extending south into the SH in central Africa, interrupting the continuity of the 200 m field at the equator.

Away from the equator, there is a rapid meridional change in s_0 at 30°S and another at 25°N . The NH strong gradient shows an increase in variability from 200 m at

January 1998



April 1998

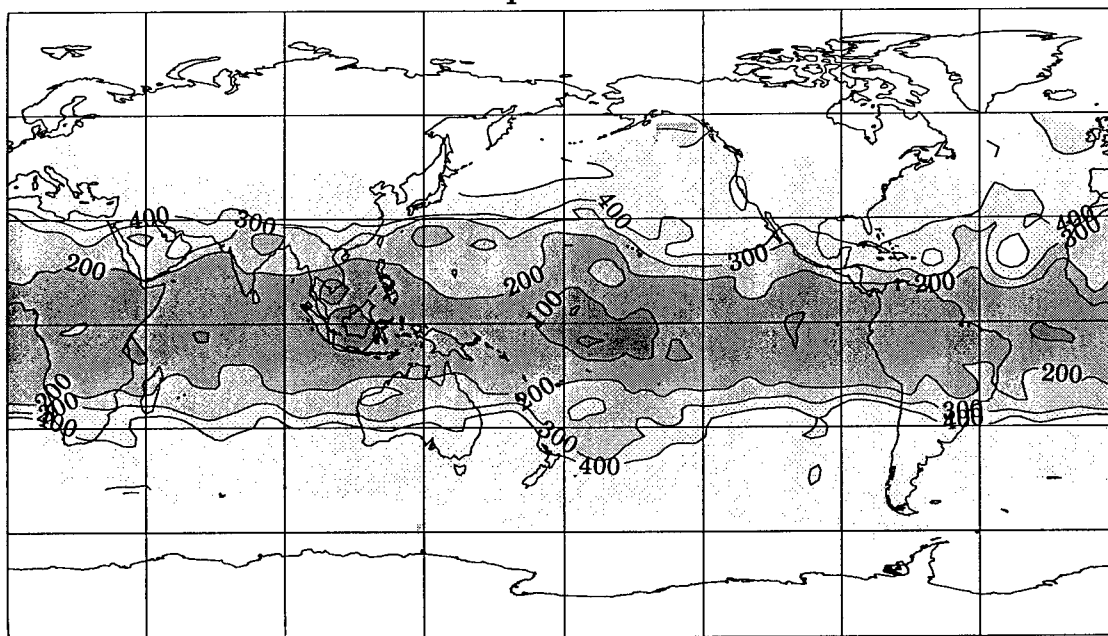
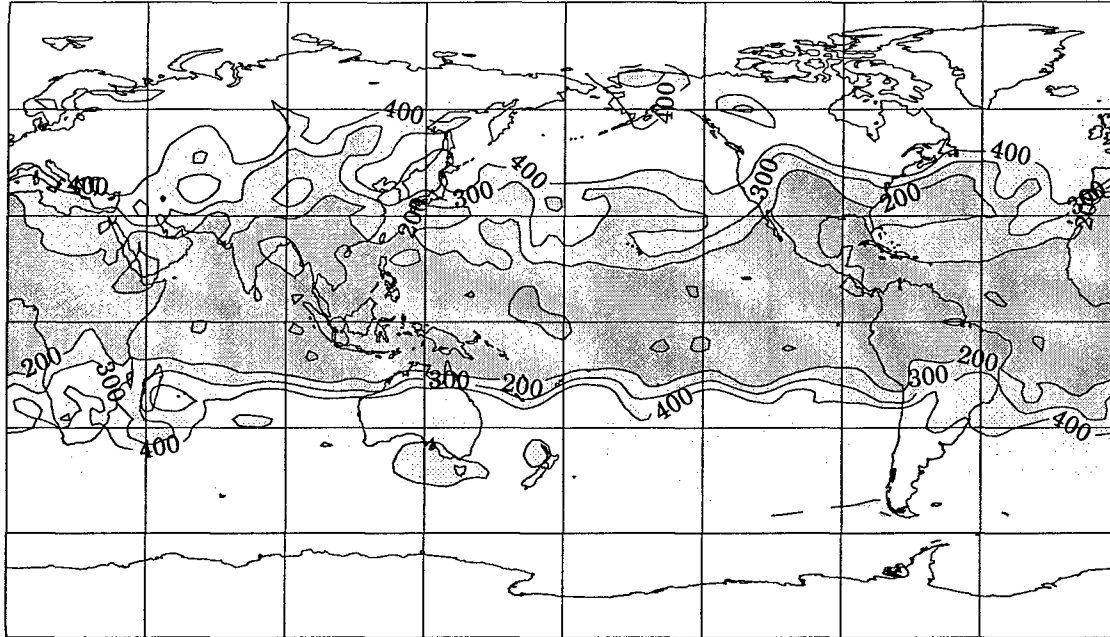


Figure 4. Intramonth standard deviation s_0 for selected months in 1998. Contours are drawn at 0, 25, 50, 75, 100, 200, 300, 400, and 500 m.

July 1998



October 1998

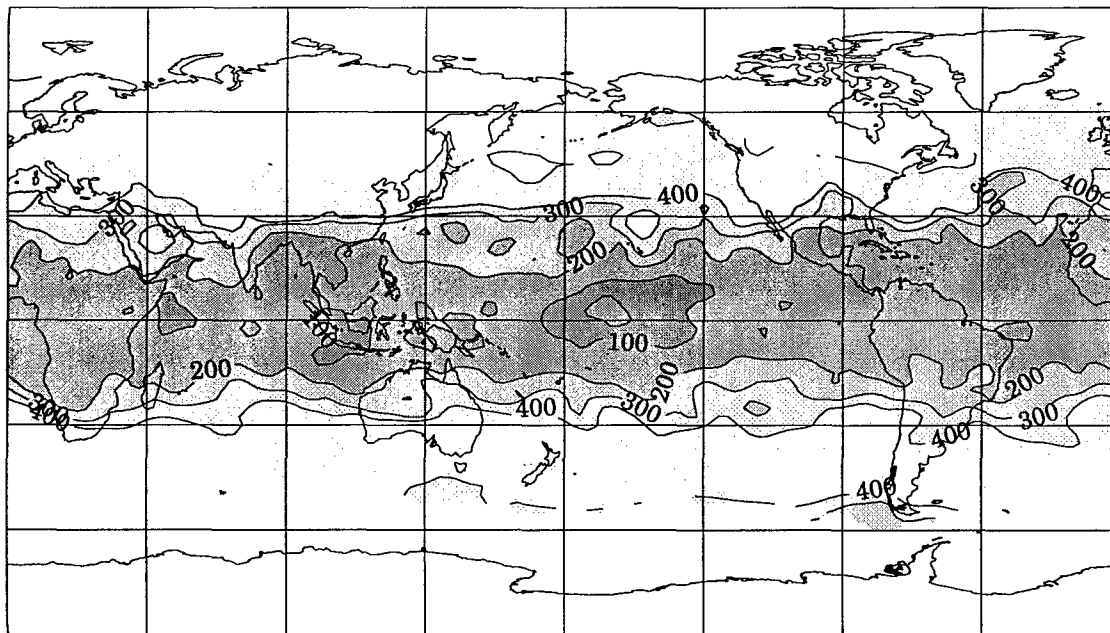


Figure 4. Continued.

about 20°N to greater than 400 m at 25°N over the western and central Pacific; the strongest meridional change in s_0 occurs in SE Asia at 125°E, 25°N. In the Atlantic, there is a strong gradient in the contours, but more variability than in the Pacific. A smooth field of > 400 m s_0 is centered around 35°N and 40°S. At 60°N, the variability decreases again, with 300 m and 200 m contours appearing at 60°S and over the NH Pacific at 45°N.

3.4.2. April. The 200 m field around the equator narrows noticeably from January, showing effect of stronger equatorial solar input due to the equinox. The basic pattern of the contours continues, with a wide band of 200 m values around the equator, 400 m in the mid-latitudes, basically zonal orientation, and increasing s_0 as latitude increases.

The pattern is generally more variable in April. While the NH variability is increasing in the s_0 field, the SH s_0 field is becoming more smooth. In comparison to the western Pacific contours in January, April's s_0 has much greater meridional variation. The lowest variability is centered on the equator in the central Pacific, with >100 m s_0 and two small areas of 75 m s_0 . However, moving away from the equator, variability is increasing in the tropics as the 100-200 m field narrows from January. The 200 m contour is about 5°-10° closer to the equator in April than in January in the NH. In the mid-latitudes, the band of > 400 m s_0 dominates at 35°N and 45°S, similar to the pattern in January. In the high latitudes, the lower variability region at 60°S disappears. In the NH, there is more southward extension of the 400 m field over the eastern Pacific and over the Atlantic Ocean south of 30°N.

3.4.3. July. Figure 4 shows the entire s_0 pattern has shifted to the north, and the increasingly variable pattern in the NH continues to show substantial deviation from

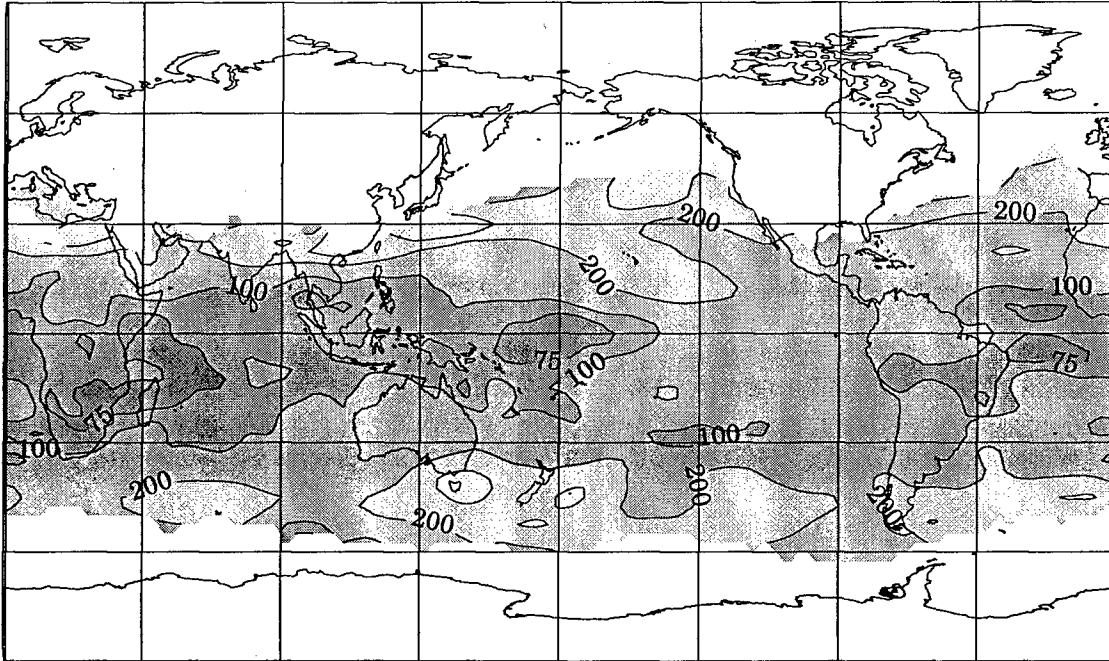
zonal, especially over Asia. In the SH, the contours represent a very smooth s_0 field. Notice also that warmer temperatures in the NH have caused an expansion of available data in the NH over Greenland, stretching almost to the poles. As before, the 400 m field dominates much of the mid-latitudes and higher latitudes, while the 200 m remains in force in the tropics. Missing data (a result of the increasing influence of cold air) dominates in the winter hemisphere above 45°S.

3.4.4. October. With some minor exceptions, the October s_0 plot shows a similar distribution to April, most likely due to solar insolation effects associated with the equinox. October in the higher latitudes of the NH brings the obvious return of cold air, with large blank space apparent at and above about 45° over land areas and 60°N over ocean due to missing data. The 200 m contour remains dominant in the tropics, with some areas of lower variability around the equator in the central Pacific and over Oceania. The 400 m contour maintains a zonal pattern around the globe at 35°N and 40°S, and increasing variability in the SH and decreasing variability in the strong gradient region in the NH. In the SH, the high-latitude change back to lower variability shows up again, with 300 m values appearing just south of Tasmania across to Chile, and some 200 m values appearing south of Cape Horn.

3.5. Interannual Variability of Monthly Means

Overall, Figure 5 shows the S_0 field is smoother than the s_0 field, reflecting the influence of the monthly mean values used in the calculation. The values of S_0 range from 50-100 m around the equator to as high as 400 m at 60° latitude in the winter hemisphere. Since areas where no freezing level exists are flagged as missing data, many areas appear blank, especially over land and in the high latitudes over ocean during cold seasons.

January 1979-1998



April 1979-1998

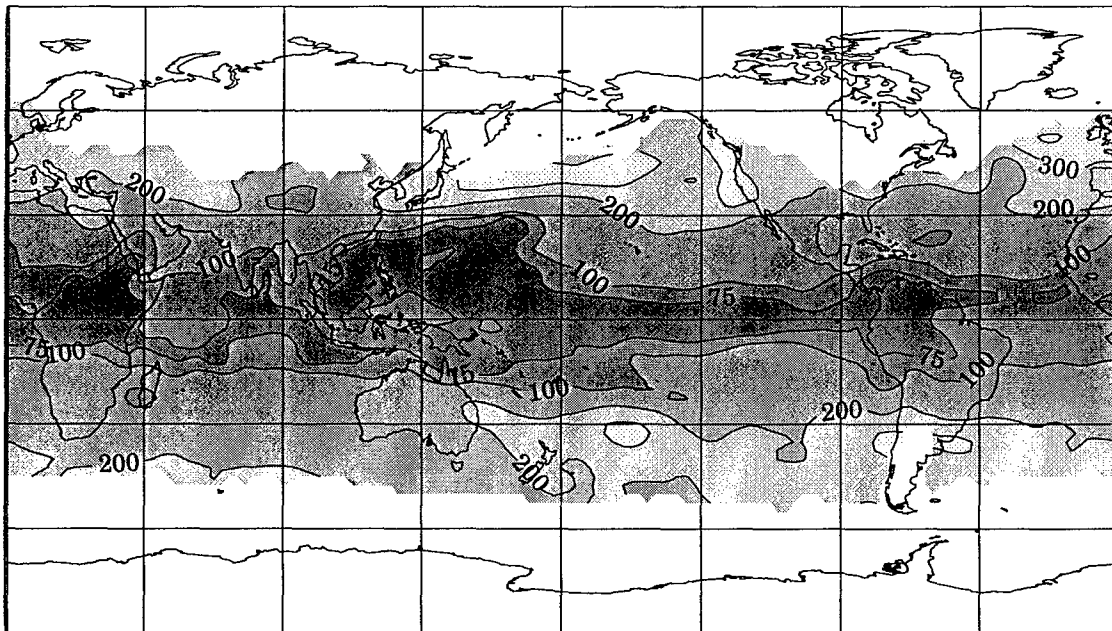
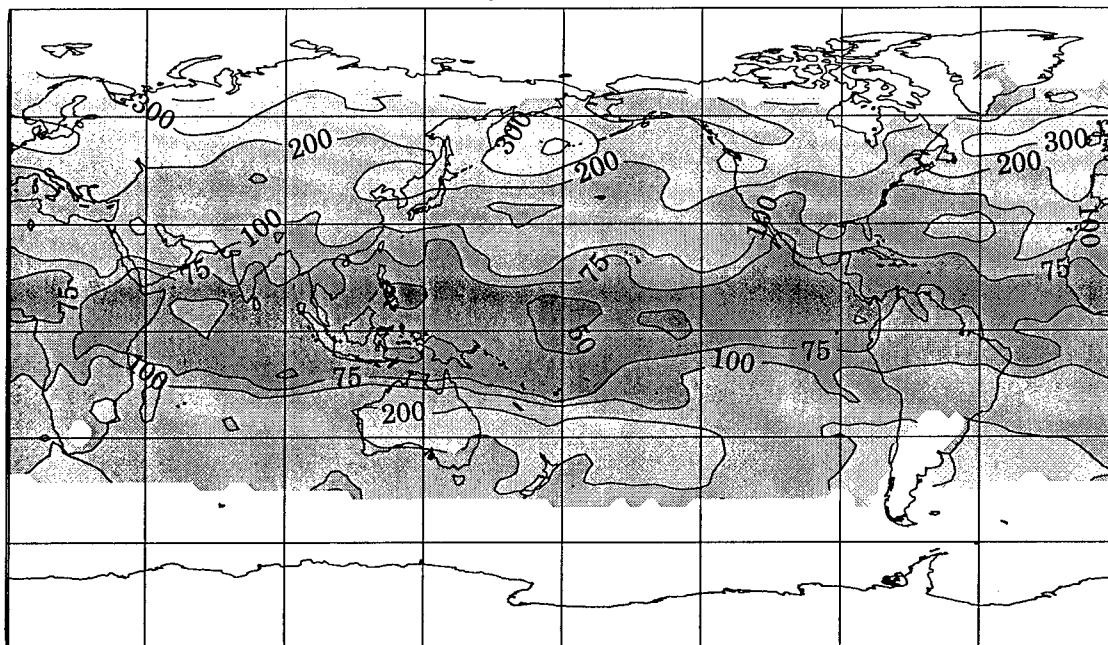


Figure 5. Interannual standard deviation S_0 for selected months. Contours are drawn at 0, 25, 50, 75, 100, 200, 300, 400, and 500 m.

July 1979-1998



October 1979-1998

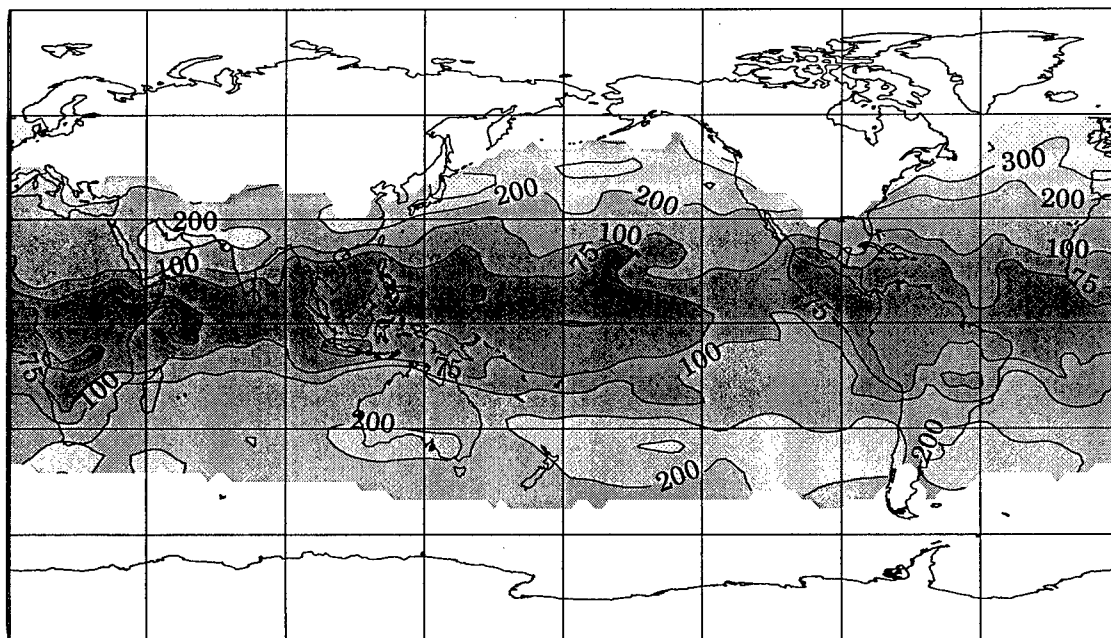


Figure 5. Continued.

3.5.1. January. In January, along the equator, a nearly continuous broad band of 100 m S_0 extends zonally from eastern South America across the Atlantic, breaks briefly over Africa, then continues across the Indian Ocean into the central Pacific. Inside this 100 m region over the Indian and Pacific the minimum variability occurs, with closed contours of 75 m, over the equatorial E Indian Ocean, central Pacific, and central Atlantic. Generally, the contour pattern in the NH shows stronger gradients over N Africa, the Middle East, and off the coast of SE Asia, and generally more variability in the NH than the pattern in the SH.

The 200 m contour in the circles the globe at 30°-35°S and 25°-30°N, defining a rather wide 100-200 m field which starts in the central and eastern Pacific and continues through into the Atlantic. The broad region of 100-200 m values dominates the tropics, extending around the equator from 30°S to 25°N. The 200 m reappears in the SH showing lower variability as high as 60°S. Some 300 m regions appear in both the NH and SH; the 300 m region in the NH is seen at 30°N and is interrupted by missing data over land. In the SH, the two small 300 m closed contours are seen at about 35°-40°S. The 300 m contours represent the highest value in the S_0 field in January.

3.5.2. April. Around the equator, variability decreases in April as the 75 m field expands meridionally to cover a wide area over the western Pacific and Oceania and zonally, extending nearly around the globe. This lower-variability field forms a narrow band around the equator of about 10° width over the central and eastern Pacific and Indian Oceans, and expands again over South America. The 100 m contour band generally follows the 75 m contour, while the 100-200 m field dominates in the equatorial W Indian and central Atlantic Oceans.

In the tropics, from about 35°S to 30°N, 200 m values stay fairly constant in width and zonal orientation. In the NH the character of this field is quite different, with a narrow corridor over the north Pacific, broadening near the eastern NH Pacific, narrowing again over North America, and broadening again over the NH tropical Atlantic. The tropics are again dominated by 75-200 m standard deviation values.

Several closed or semi-closed 300 m contours are found in the higher latitudes. In the SH, the closed 300 m S_0 areas are found over extreme southern South America and in the central SH Pacific Ocean. In the NH, a broad area of 300 m values extends into the north Pacific, and another 300 m closed contour runs north-south along the California coast. The maximum value is found in the north Atlantic at 15°W, with a small closed contour of 400 m S_0 values.

3.5.3. July. Figure 5 shows the July S_0 equatorial low-variability region shifts to the north and expands in meridional coverage. Much more data appears in the high latitudes of the NH, indicating infrequent occurrence of 0° C over the NH continents. Additionally, the first appearance of the < 50 m S_0 field occurs in July, as 50 m contours appear along the equator in the central Pacific, Oceania, and the Indian Ocean. This is the lowest variability in the climatology data set.

The broadening 75 m S_0 field extends over the western equatorial Pacific and Indian Oceans, and continues to grow in meridional extent around the globe. The only break in the field occurs in central Africa, at about 25°E. This growth in the 75 m field is likely related to the increased sensible heat generated by the continents in the NH, because the SH summer does not produce the same type of pattern in the low-variability region in the tropics.

In the midlatitudes of the NH, the 100-200 m field continues to dominate at 30°-35°N. In the SH, the 100-200 m field dominates from about 15°S to 45°S, with some intermittent closed 200 m contours. Unlike the NH, where a strong band of > 200 m values extends around the globe at 35-40°N, the SH 200 m field is much weaker, appearing as two large discontinuous areas at 30°S.

In the higher latitudes, the 300 m contour appears much stronger in the NH; in fact, there is only one small appearance of the 300 m field in the SH at 35°S, 140°W. The austral winter, in contrast to the boreal winter, does not show the same pattern of variability. In the NH, winter cooling induces 400 m standard deviation values, whereas the SH has almost no strong variability in the winter; even the pattern of missing data is zonal, with the exception of the deviation north over southern South America.

3.5.4. October. April and October, as with the intramonth standard deviation maps, are remarkably similar. Fall in the NH brings an obvious change: fewer contours are seen over land as the entire standard deviation field shifts toward the south. Whereas the summer months had significant data over land, the fall has enough occurrence of freezing weather – as far south as 30°N – that cold weather causes missing data over much of the NH continental areas.

In October, the 50 m S_0 field returns in the Indian and Pacific Oceans. In the Indian Ocean, this feature extends in a narrow band from Africa across Oceania to the Philippines. The 75 m field, though smaller in meridional extent, still runs nearly all the way around the globe at the equator, very similar to the pattern of 75 m S_0 in April.

The 100-200 m field increases southward in the Pacific in the NH; similarly, the 100-200 m region widens and pushes farther south in the Atlantic. Taken together, the 75-

200 m S_0 field is the dominant range of values throughout the tropics, and extends as high as 30°S and 30°N.

In the SH, the growth of the 200 m closed S_0 contours is apparent at 45°S. Several other closed contours at or near 45°S appear at different longitudes, but in general the 45° latitude is characterized by the 200 m S_0 field. In the NH, the 200 m S_0 field is a narrow band around the globe at 30°N. A couple of areas of 300 m values exist in the SH, one off the S coast of New Zealand, the other southwest of the Cape of Good Hope in Africa.

3.6. Cross-Sectional Plots of the 1979-1998 Zonal Mean

Figure 6 shows cross-sectional plots of the 1979-1998 climatological zonal mean, $\langle \overline{Z_0} \rangle$. The axes show height in meters versus latitude. The value is calculated by taking the $\overline{Z_0}$ values, summing around a latitude circle, and dividing by the number of gridpoints (73 on the NCEP grid). S_0 is plotted as error bars on the curve.

3.6.1. January-February-March. These plots show the effect of cold weather over the continental NH as the curve terminates between 25°N and 30°N in each graph. When the data is contoured, no contour is drawn in the case of missing data. In the SH summer, the contours extend much further into higher latitudes. This indicates above-freezing temperatures at the surface over most of the mid-latitudes, as expected in the warm season. It is seen from the plot that the S_0 increases with latitude, and $\overline{Z_0}$ decreases with increasing latitude. The minimum S_0 is not found centered on the equator, but rather just south of the equator at about 7°S. The “dome” of maximum $\overline{Z_0}$ extends from ~20°S to ~15°N.

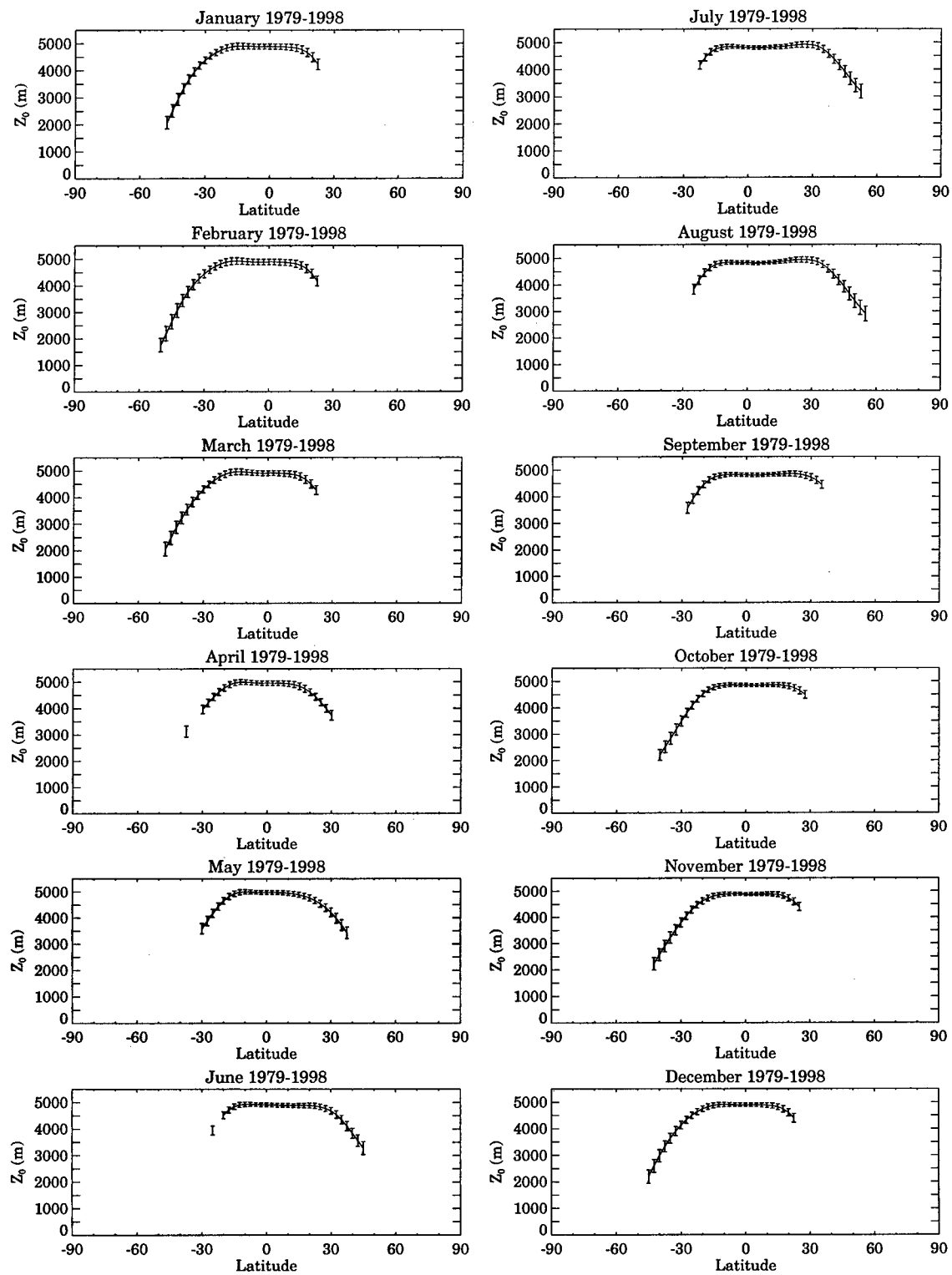


Figure 6. Zonal cross sections of $\langle \overline{Z_0} \rangle$ for each month. Error bars are standard deviation values. Missing data causes the truncation of the curves.

3.6.2. April-May-June. As the NH moves into spring, the plots show the response of $[\overline{Z}_0]$ as more data is available on the map farther north as boreal spring begins. In the SH, the curve truncates to the south as austral summer ends and fall begins, with colder surface temperatures resulting in an increasing number of gridpoints with missing data in the higher SH latitudes. At the equator, as is expected, the values for the $[\overline{Z}_0]$ and S_0 are stable; the minimum S_0 shifts back to the equator in April-May, but then begins a move into the NH in June. Also in June, the “dome” of the curve shifts to the north, hitting the maximum curvature point at 25°N , as opposed to $15^\circ\text{-}20^\circ\text{N}$ in the previous panels. The SH maximum curvature point occurs at 15°S , a move of 5° from January. This broadening trend continues into the NH summer.

3.6.3. July-August-September. This period shows the movement of equatorial-type $[\overline{Z}_0]$ to the north. In July and August, the maximum curvature point – showing the northward extent of equatorial-type $[\overline{Z}_0]$ – reaches north to just past 30°N . September shows the extended area of equatorial $[\overline{Z}_0]$ beginning to recede back toward the tropics, with maximum curvature at 25°N . Minimum S_0 shifts from near the equator in May to 10°N , where it stays through August.

The truncation of the SH $[\overline{Z}_0]$ curve reaches a maximum in the middle of July during SH winter, and is similar to the January plot from NH winter. One interesting difference here is that the NH $[\overline{Z}_0]$ are higher than their SH seasonal counterparts. The NH August $[\overline{Z}_0]$ at 55°N is on the order of 3000 m, while in SH, for February, the same value is much lower, reaching only 1800 m.

3.6.4. October-November-December. The last three months are nearly identical in shape to January, February, and March. The exception is that the “dome” of

equatorial maximum $[\overline{Z}_0]$ shifts back to the south and narrows, reversing the summer broadening effect. As the broadening effect reverses, the movement of the minimum S_0 from the north back to the south also continues, as the minimum S_0 region ends up back in line with the equator by December.

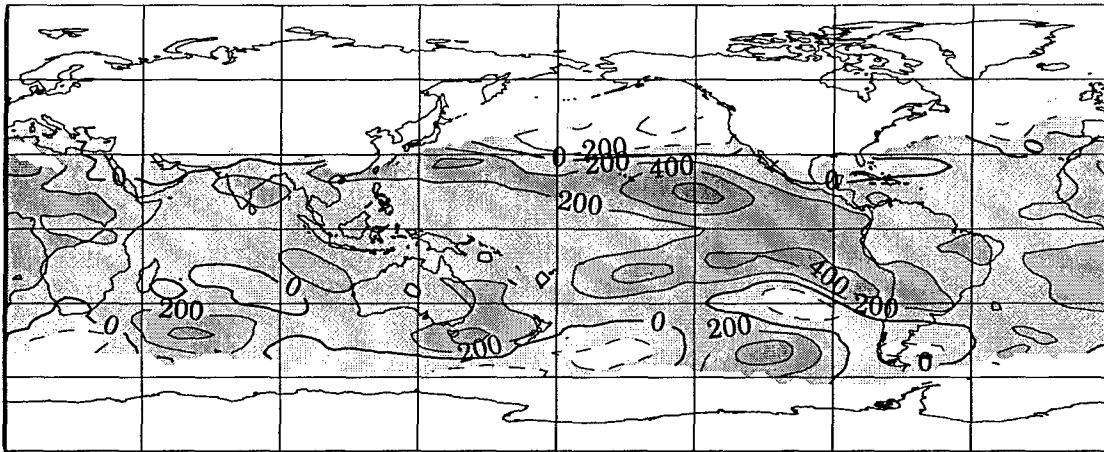
3.7. Freezing Level Anomalies for 1998

Figure 7 shows the \overline{Z}_0 anomalies from 1998. Contours are drawn every 200 m starting at -800 m, with a maximum value at $+800$ m. Negative contours appear as dashed lines and lower values have lighter fill shading. The zero contour line is 2.5 times thicker than the other contours for emphasis.

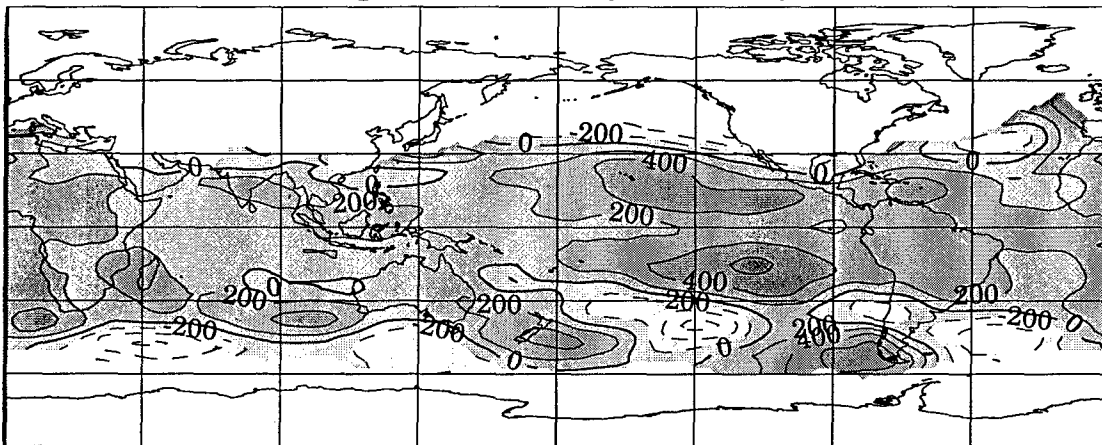
3.7.1. January-February-March. Overall, February shows the most variation in \overline{Z}_0 . In general, the maps show a basically zonal distribution of higher than usual \overline{Z}_0 across the entire tropics, with values ranging from 100 m to > 200 m over most areas. Anomalies in the tropics reach as high as > 600 m in dual maxima straddling the equator in the eastern Pacific during January and February. In the NH mid-latitudes and in the SH upper mid-latitudes, negative anomalies are more prevalent. Several areas of low \overline{Z}_0 exist at $\sim 35^\circ\text{S}$ and higher over the extreme south Atlantic, south-central Pacific, and south Indian Oceans in February. In the NH, there are also negative anomalies above 30°N . Positive anomalies appear again in the SH at very high latitudes, with a > 600 m region off the Cape of Good Hope in S South America in February.

3.7.2. April-May-June. Generally, the zonally-oriented, slightly positive (100-200 m) anomaly field continues. A disturbed pattern in the mid-latitudes emerges during this period in the NH especially, and to a lesser extent in the SH, over the Pacific Ocean.

Freezing Level Anomaly, January 1998



Freezing Level Anomaly, February 1998



Freezing Level Anomaly, March 1998

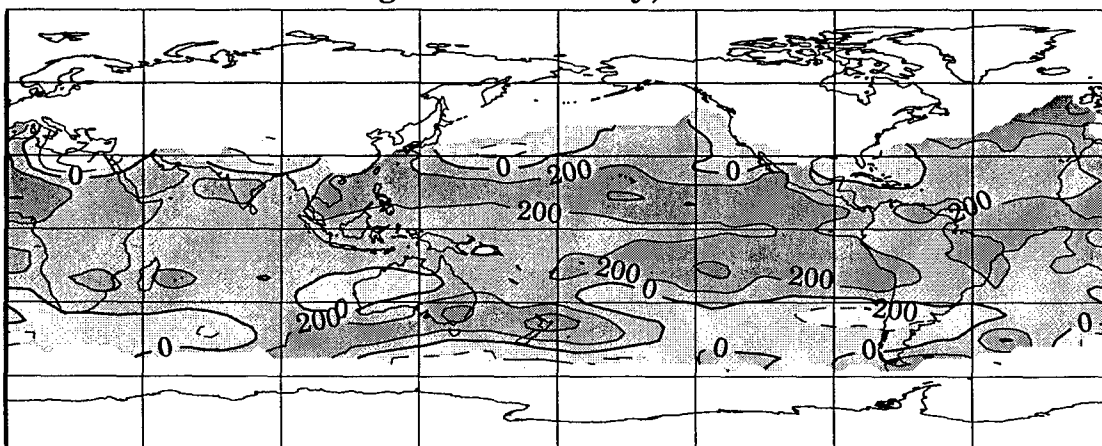
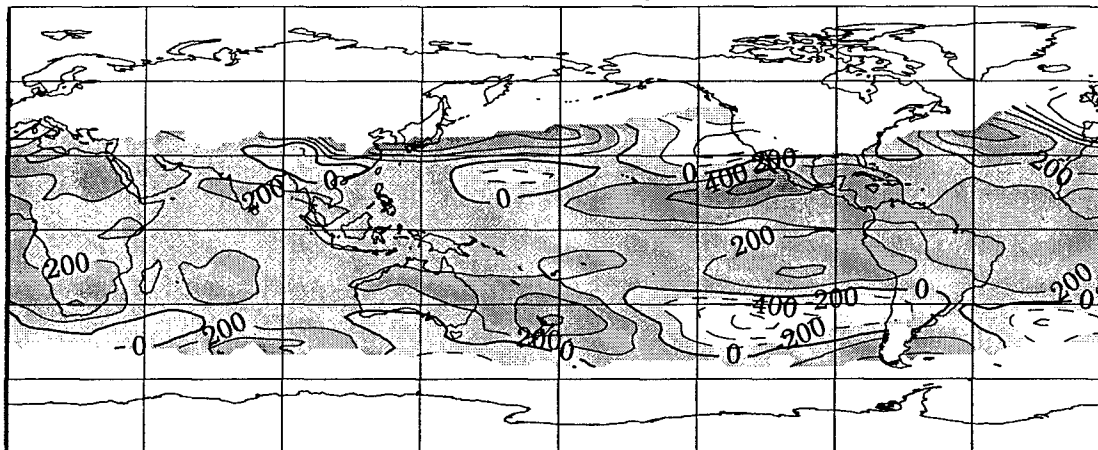
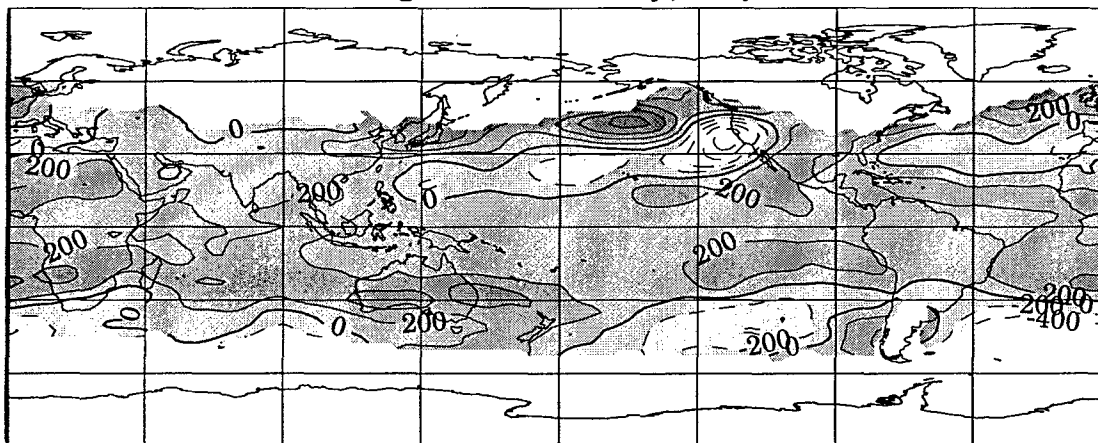


Figure 7. 1998 anomalies maps for \bar{Z}_0 . Contours are drawn every 200 m, starting at -800 m and going to +800 m.

Freezing Level Anomaly, April 1998



Freezing Level Anomaly, May 1998



Freezing Level Anomaly, June 1998

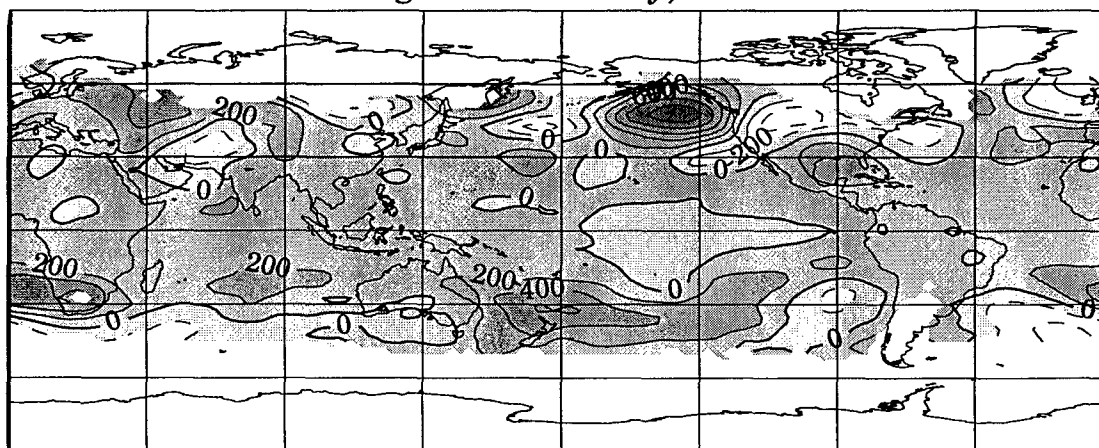
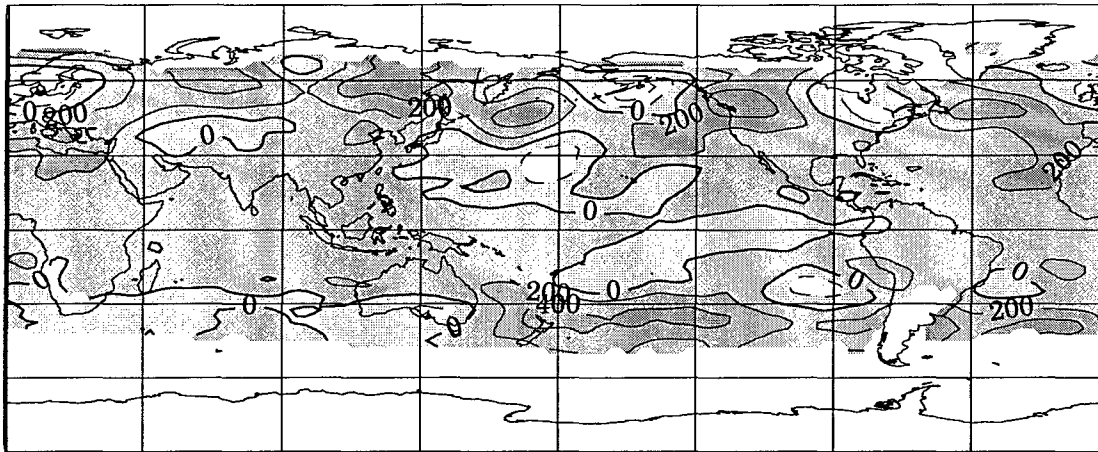
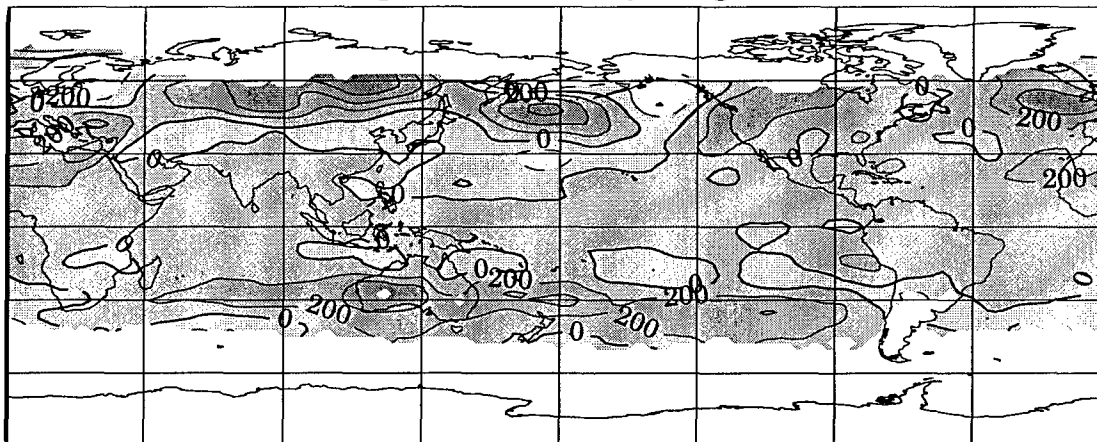


Figure 7. Continued.

Freezing Level Anomaly, July 1998



Freezing Level Anomaly, August 1998



Freezing Level Anomaly, September 1998

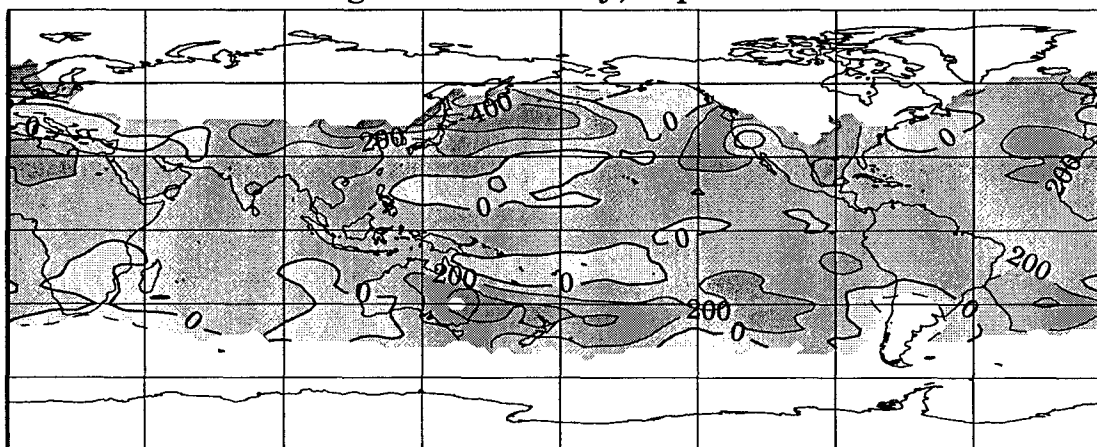
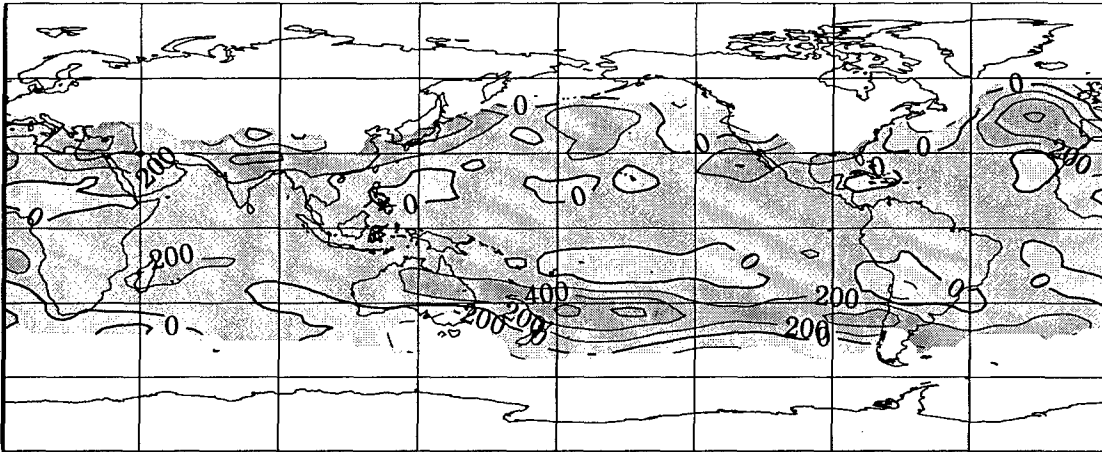
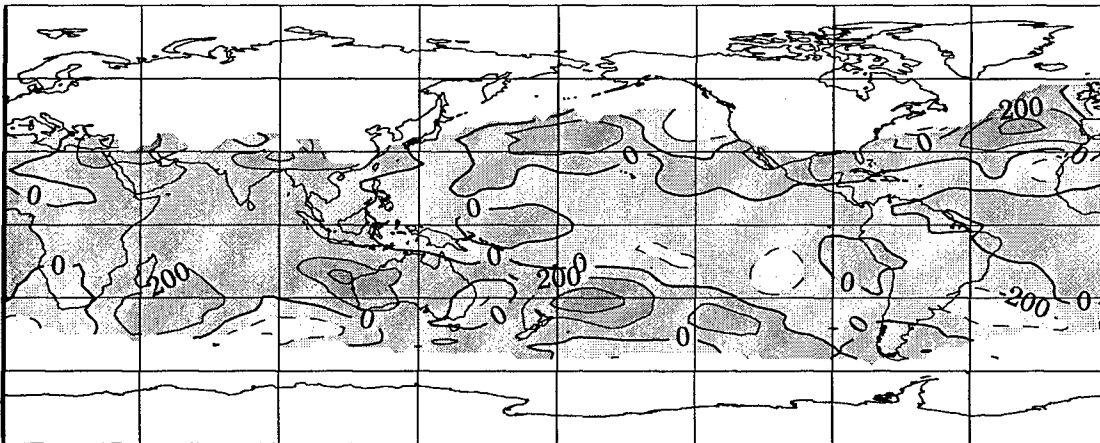


Figure 7. Continued.

Freezing Level Anomaly, October 1998



Freezing Level Anomaly, November 1998



Freezing Level Anomaly, December 1998

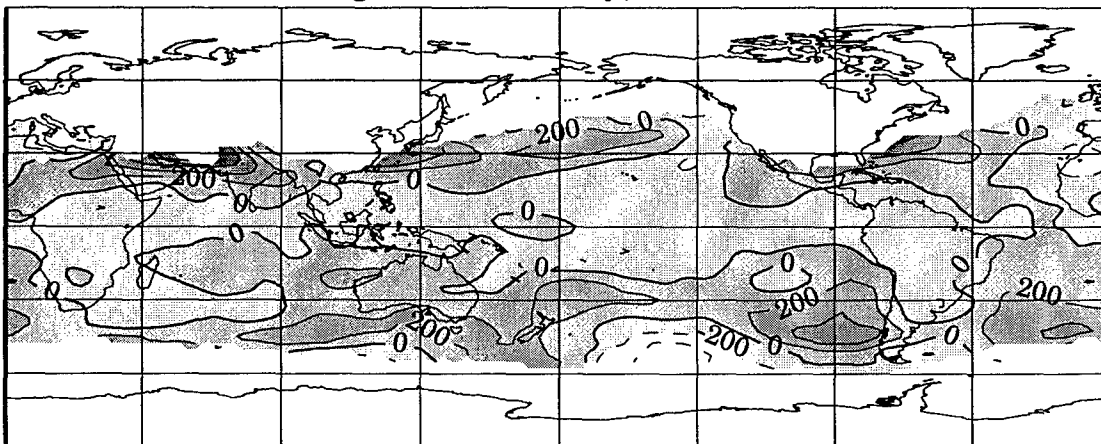


Figure 7. Continued.

An area of very high anomalies (> 600 m) develops over western Pacific at $\sim 30^{\circ}\text{N}$ in April, with an area of low anomalies (< 200 m initially) over the central and western Pacific. In the SH, a < -600 m anomaly at 35°S is apparent but decreases through the period. The NH minimum anomaly feature reaches its lowest value at < -800 m in May, and extends from the Philippines into the Rocky Mountains of North America. The NH maximum anomaly is located in the north central Pacific. The minimum anomaly area stretches into the Atlantic and Europe, with a minimum over the Atlantic and Europe. The minimum over Europe is of lower magnitude than the region over the United States. The positive anomaly maximum reaches its highest value (> 800 m) over the Gulf of Alaska in June as the minimum anomaly stretches over the North American continent from the eastern Pacific into the Atlantic.

In the central Pacific, the dual-maxima feature from the first three months of 1998 weakens through the period and disappears by June. A positive anomaly (> 600 m) north of New Zealand maintains its location and intensity through the period.

3.7.3. July-August-September. Throughout the tropics, the anomaly field changes very little in this time; the anomaly field in the tropics has values 0-100 m for the entire period. The areas with the most variation are found in the mid-latitudes, as in the previous period, yet the intensity is much lower as there are fewer maxima and minima features. The minimum values in July are < -200 m, while the maximum values reach > 600 m in the north Pacific and over northeast Asia in August.

3.7.4. October-November-December. Cold air returns to the NH in this period, as the increase in missing data over the continental areas indicates. Generally, the trend toward a more-quiet anomaly pattern continues from the previous period, as the tropics

remain in the range of 0-100 m. The mid-latitudes continue to show the most deviation from climatology, with maximum values in the > 600 m range in the NH over SW Asia in October, and minimum anomalies of < -400 m in the far south Pacific.

3.8. Comparison Part I: Difference Maps

A comparison of the retrieved \overline{H}_0 to \overline{Z}_0 for 1998 is shown in Figure 8. Each plotted box represents $10^\circ \times 10^\circ$ area and is plotted with a grayshade, proportional to the magnitude of the difference $\overline{H}_0 - \overline{Z}_0$, using the scale from -2100 m to 1200 m given at the bottom of the page. The scale bar has eleven 300 m intervals for the grayshades. Darker values indicate \overline{Z}_0 is greater than \overline{H}_0 and vice-versa. This box-plot method follows Shin's (personal communication, 1999).

The range of plotted values for the year is -2073 m to 1103 m. Each month's range of plotted data (minimum and maximum values) are presented in Table 1. It is apparent that the difference between the two fields is usually within a few hundred meters; the total mean difference over all the data is around 600 m. Figure 8 does not show any clear zonal pattern, as does the more-continuous NCEP \overline{Z}_0 field; clearly the missing data and short sampling period hamper the analysis.

The continental areas in the winter hemisphere show the effect of cold temperatures, with the expected regions of missing data over continents. In the first half of the year, during austral summer, the data shows much better continuity in the SH than in the NH. As the year progresses, data coverage in the NH improves substantially. Generally, if data is missing in the sub-tropics and/or over land, cold temperatures are likely to be the cause; near the equator and over oceans, lack of precipitation is more likely the cause. The most notable areas are the well-known dry regions off the west

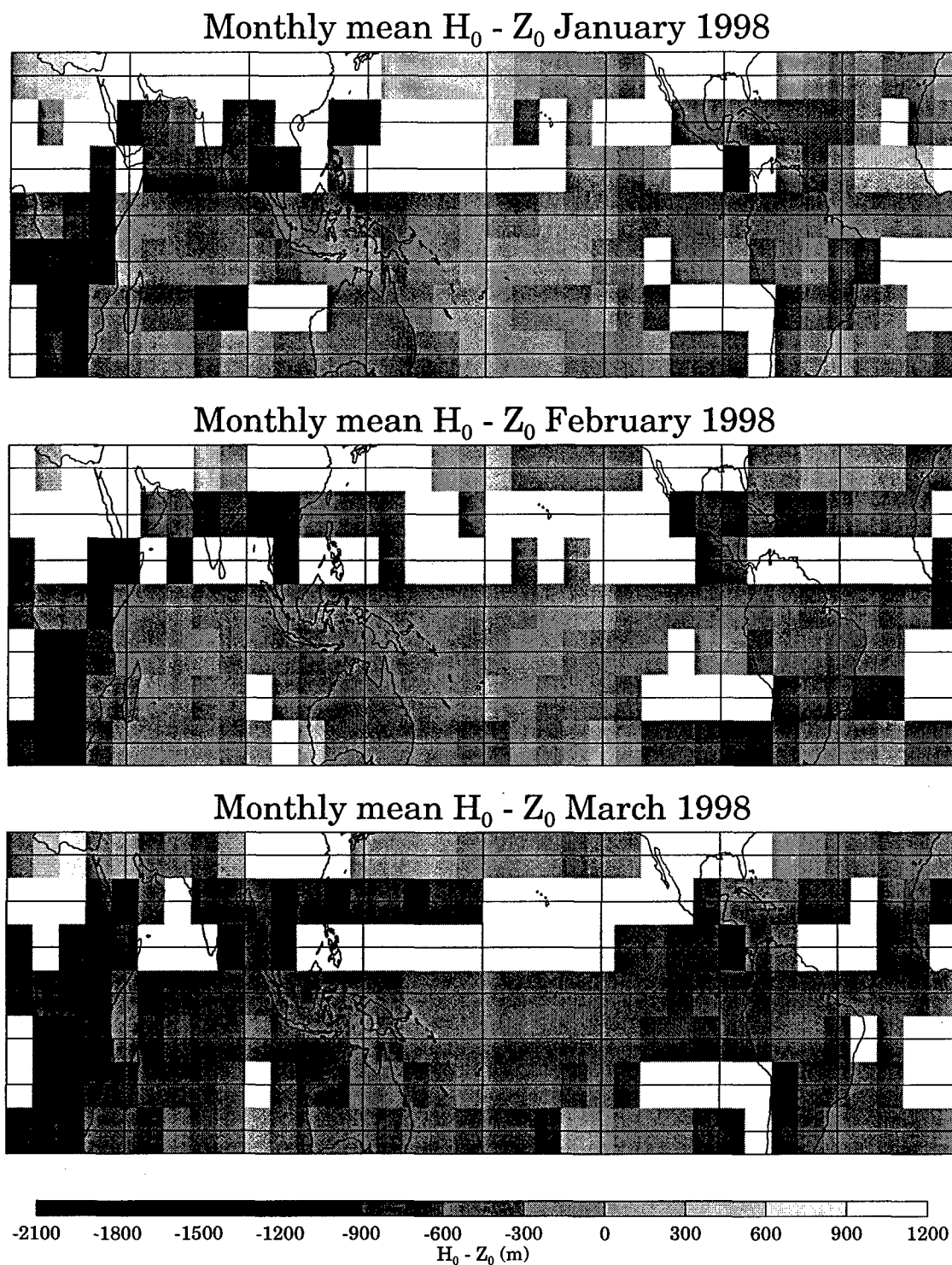


Figure 8. Monthly raw differences between $\overline{H_0}$ and $\overline{Z_0}$. Bar scale gives interval-to-grayshade relationship. Each grid box is $10^\circ \times 10^\circ$.

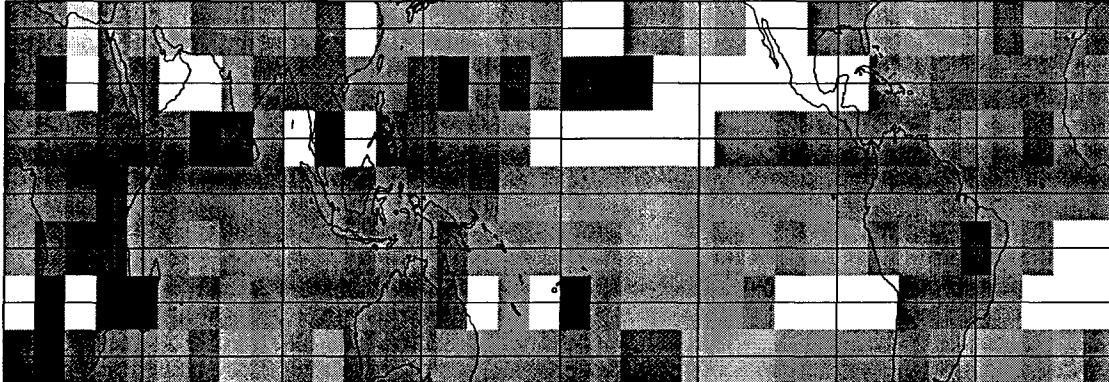
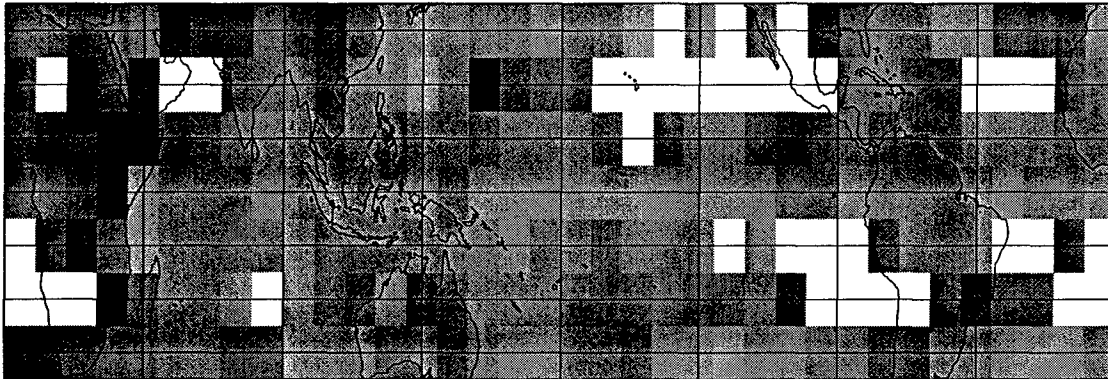
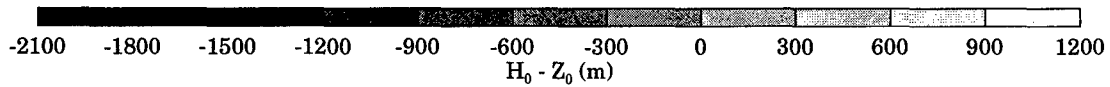
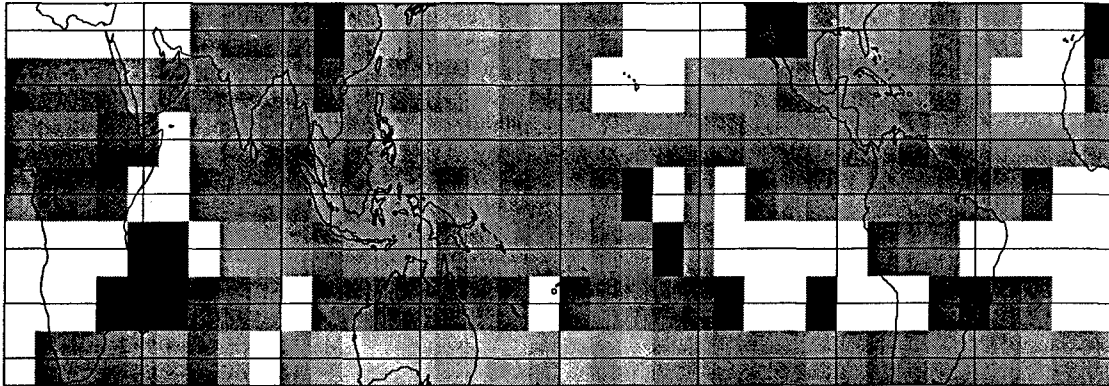
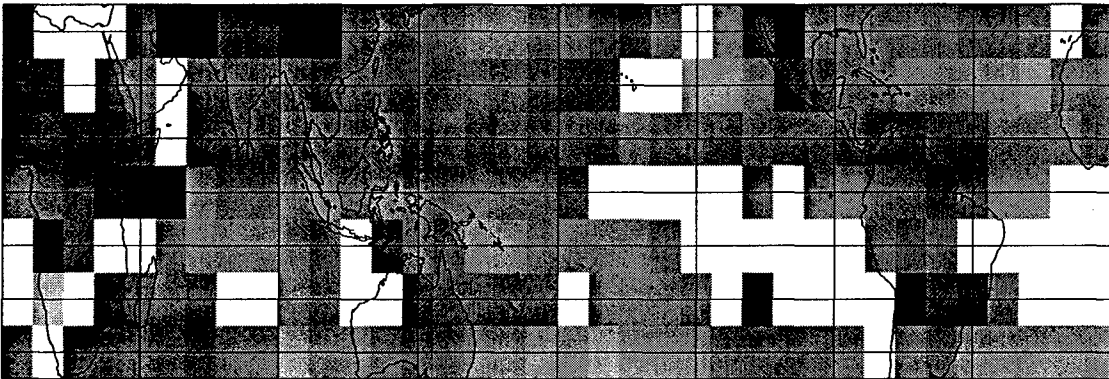
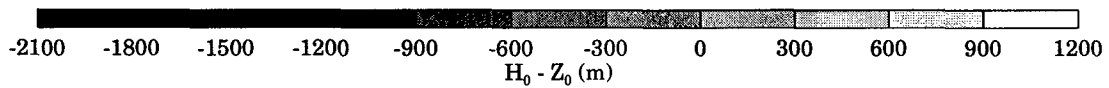
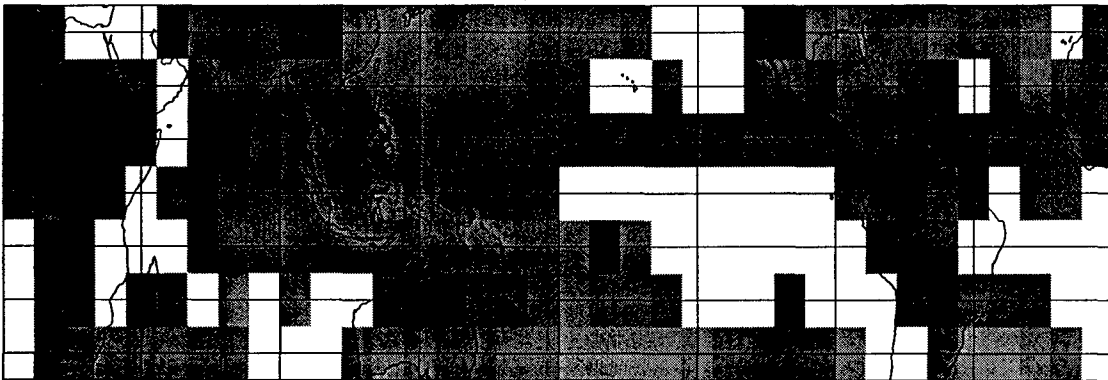
Monthly mean $H_0 - Z_0$ April 1998Monthly mean $H_0 - Z_0$ May 1998Monthly mean $H_0 - Z_0$ June 1998

Figure 8. Continued.

Monthly mean $H_0 - Z_0$ July 1998Monthly mean $H_0 - Z_0$ August 1998Monthly mean $H_0 - Z_0$ September 1998**Figure 8.** Continued.

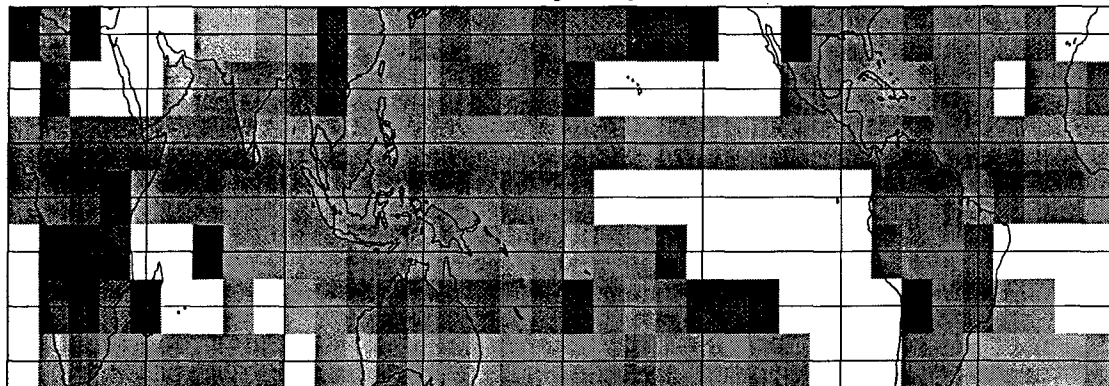
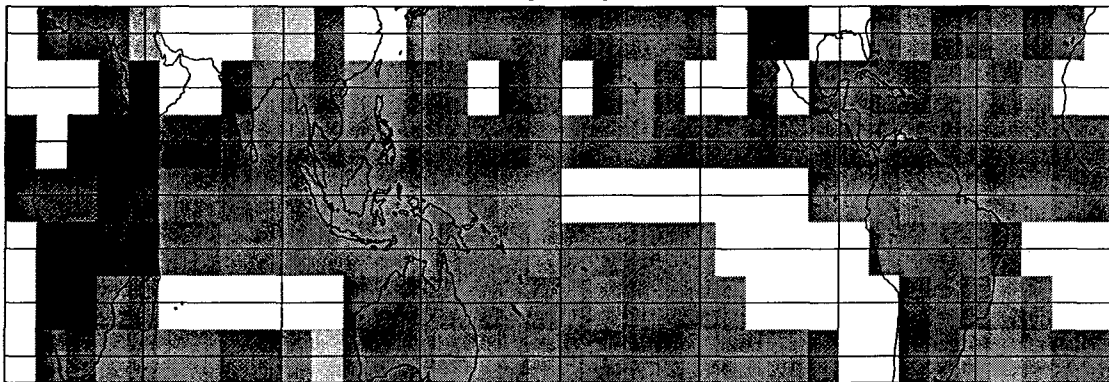
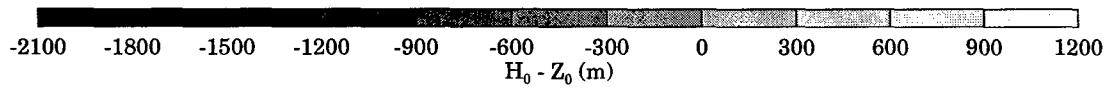
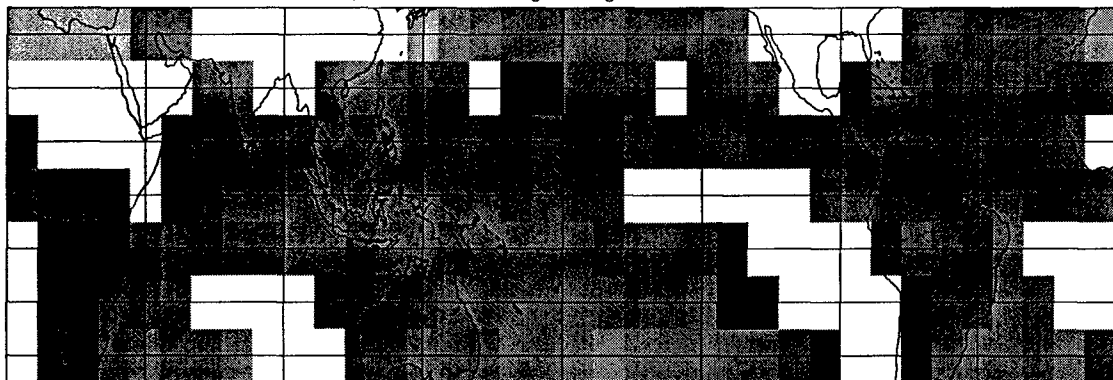
Monthly mean $H_0 - Z_0$ October 1998Monthly mean $H_0 - Z_0$ November 1998Monthly mean $H_0 - Z_0$ December 1998

Figure 8. Continued.

Table 1. Difference in \overline{H}_0 and \overline{Z}_0 and range (maximum and minimum data values) for each month in 1998.

Month	Monthly Mean $\overline{H}_0 - \overline{Z}_0$	Range, $\overline{H}_0 - \overline{Z}_0$	
		minimum value	maximum value
January	-567	-2073	417
February	-598	-1718	577
March	-493	-1906	1103
April	-569	-1983	509
May	-502	-2047	13
June	-549	-1678	51
July	-518	-2057	564
August	-515	-1781	431
September	-729	-1858	56
October	-731	-1827	56
November	-733	-2054	450
December	-687	-2056	322

coasts of the continents. This dryness manifests as large areas of missing data through the year, apparent mostly in the SH from July through the end of the year. However, these areas of missing data may well be associated with some cold temperatures (missing \bar{Z}_0 data) early in the year over land. In the tropics, \bar{Z}_0 is never lower than \bar{H}_0 , though there are some locations in and around the mid-latitudes where \bar{H}_0 is higher than \bar{Z}_0 .

Figure 9 depicts the mean difference between \bar{H}_0 and \bar{Z}_0 for the entire year. Eight grayshades (as opposed to 11 in Figure 8) are used to differentiate the eight intervals from -100 m to -1700 m. Appropriately, the mean difference is always negative, indicating the expected higher magnitude of \bar{Z}_0 . A few other features are notable. First, the only "year-long" dry regions are in the SH off the coasts of Africa and South America. Second, over oceans, the differences tend to be somewhat smaller than over land, in the tropics and SH. Open ocean regions typically show differences in the -100 to -500 m range. Over land, the differences are substantially larger, especially over Africa. Third, some regions of higher differences occur near the "dry" regions off the west coasts of Africa and South America; these areas are most likely related to low number of samples in that area. Finally, two bands of higher differences appear at 20°N and S; these areas of higher differences are most well-defined over the Pacific.

3.9. Comparison Part II: Zonal Means Cross-Sections

Figure 10 shows the relationship between $[\bar{H}_0]$, $[\bar{Z}_0]$, and $[\langle\bar{Z}_0\rangle]$. The plot shows that $[\bar{H}_0]$ and $[\bar{Z}_0]$ shift toward lower values over time. For example, the January $[\bar{Z}_0]$ curve is well above climatology; but by the last quarter of the year, $[\bar{Z}_0]$ is roughly equal to climatology and nearly identical by December. It is seen that the two parameters— $[\bar{H}_0]$ and $[\bar{Z}_0]$ —move in unison. The average mean zonal difference between $[\bar{H}_0]$ and $[\bar{Z}_0]$ is around -600 m, while the range of the mean zonal difference is from about

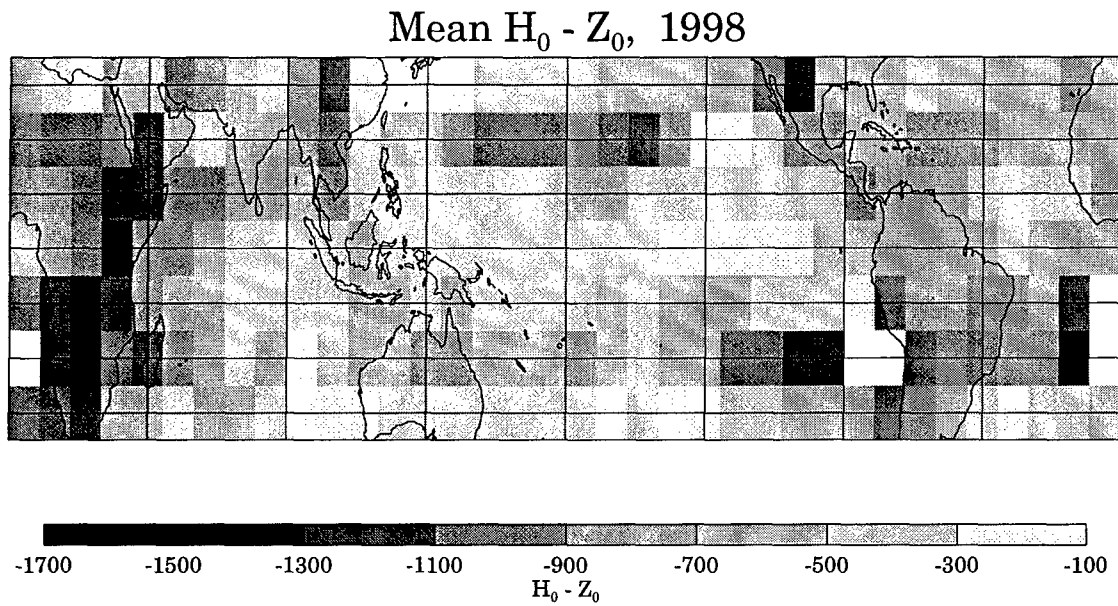


Figure 9. 1998 mean difference $[\overline{H_0}] - [\overline{Z_0}]$. The bar scale gives the interval-to-grayshade relationship.

–200 m to –1000 m. The minimum difference between the means occurs in the SH in summer and fall, where from the equator south the estimates are almost always within –300 m from January to June. The largest differences occur in the winter hemisphere, where gaps on the order of –800 to –1000 m occur in the latitudes at 20°N or S.

In the latter months of 1998, the contours show some spreading compared to earlier in the year. For example, October and April, from previous analysis of the $[\overline{Z}_0]$ field, should be relatively similar. In fact, the two show a difference between the $[\overline{Z}_0]$ and $[\overline{H}_0]$ for April and October of about –200 m in the SH and around the equator. However, looking at the graphs, the April NCEP $[\overline{Z}_0]$ does not appear to be any different from October $[\overline{Z}_0]$, while the PR $[\overline{H}_0]$ is definitely lower. A time series comparison (not shown) did not identify any significant trends in the differences through the year.

Figure 11 shows the quantity $[\overline{H}_0] - [\overline{Z}_0]$ for each month in 1998 plotted as a longitudinal cross section. Early in the year, the difference is between –300 and –900 m. The difference in the zonal means stays relatively constant in the first six months of 1998, then shows some increase in the last six months, as evidenced by the shift of the curve upward (more negative). An interesting feature occurs at 20° latitude in the winter hemisphere, as the difference “peaks” at between –600 and –800 m. Overall, the mean difference is around –600 m, slightly higher in the second half of 1998 than in early 1998.

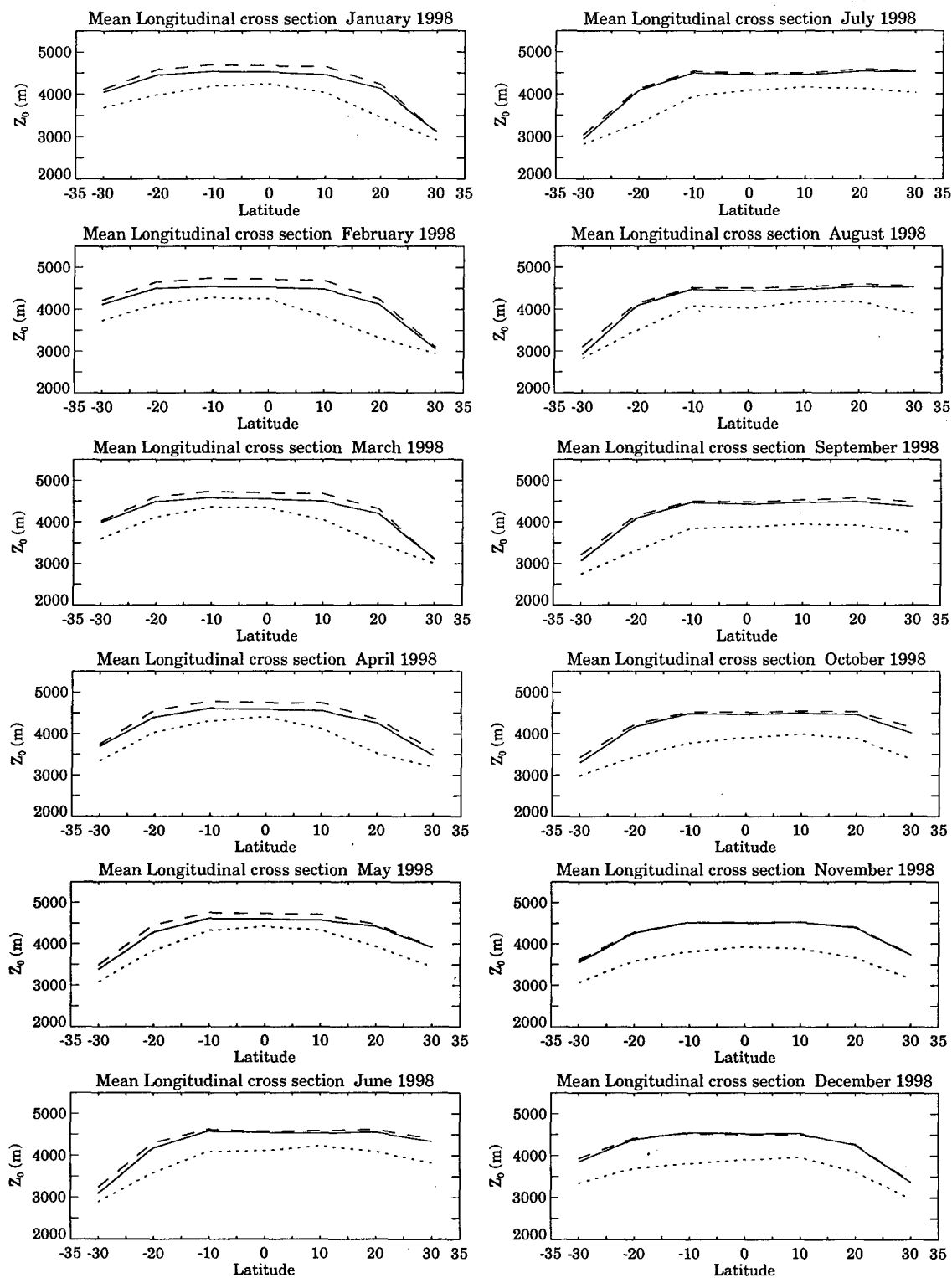


Figure 10. Cross sections of $\langle \overline{Z_0} \rangle$ (solid line), $[\overline{H_0}]$ (dotted line), and $[\overline{Z_0}]$ (dashed line) for each month.

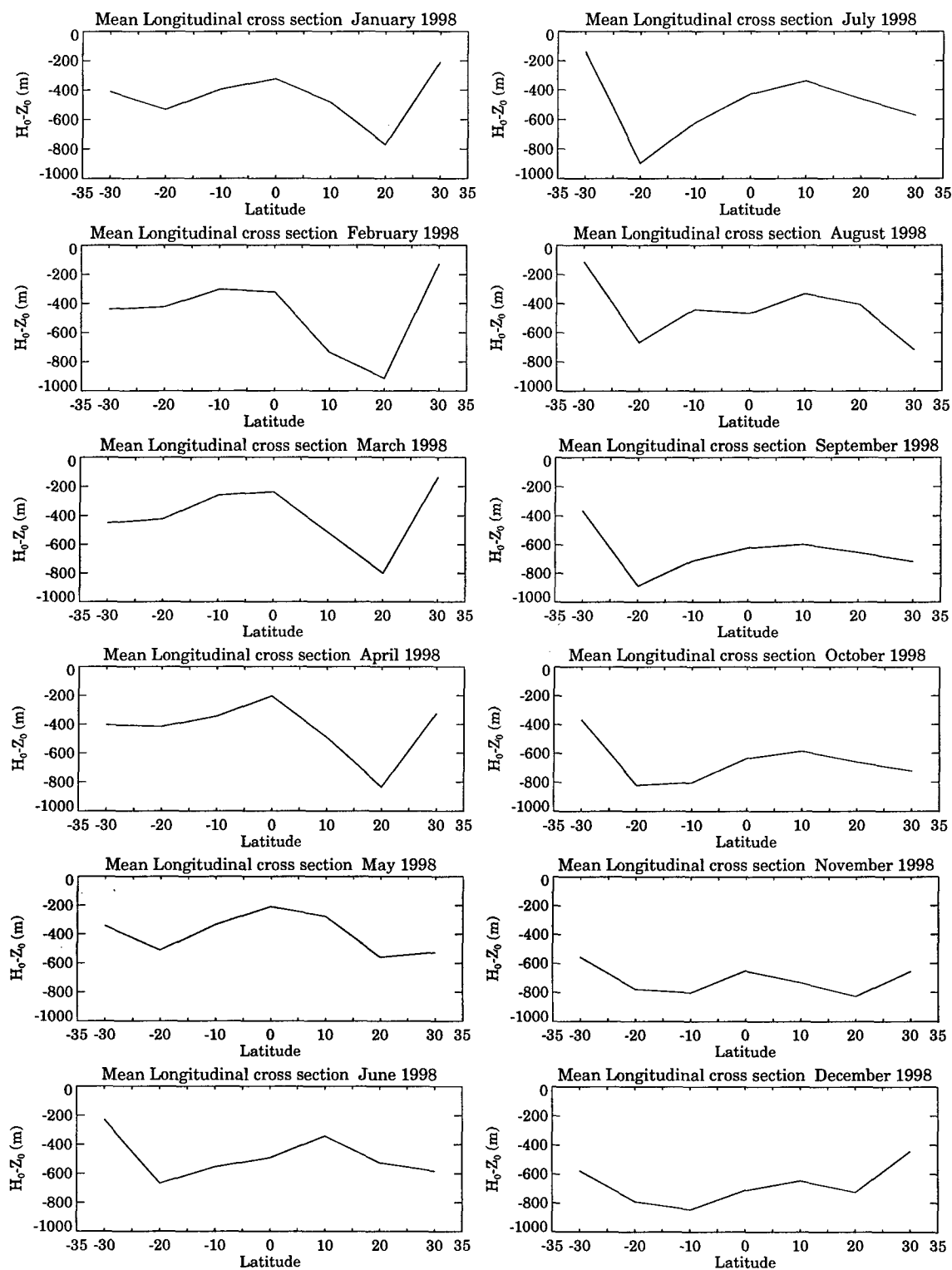


Figure 11. Cross-sections of $[\overline{H_0}] - [\langle Z_0 \rangle]$ for each month.

CHAPTER IV

SUMMARY AND CONCLUSIONS

4.1. General

The atmosphere gets three-fourths of its heat energy from the release of latent heat by precipitation, and two-thirds of this precipitation falls in the tropics [Kummerow *et al.*, 1998]. Improving the understanding of tropical rainfall is important so that climate and general circulation models can better parameterize precipitation, its associated latent heat release, and the resulting impact on the atmospheric circulation. The primary goal of the TRMM mission is to quantify tropical precipitation in space and time [Simpson *et al.*, 1988]. Much of the effort to do so will depend upon rainfall retrievals from passive microwave measurements on TRMM and future operational satellites.

The TRMM satellite package contains multiple sensors so that more than one type of data is available to “cross-reference” and more accurately determine the state of the tropical atmosphere. Rainfall retrieval algorithms for passive microwave data, for example, require accurate freezing level or melting layer estimates as an input parameter, which can be estimated using TRMM PR data. The PR melting layer retrievals given by Shin (personal communication, 1999) are one step toward better estimates of melting layer altitude. This research computes a climatology of the height of the 0° C isotherm, Z_0 , from NCEP reanalysis data, and compares TRMM PR-derived melting layer height, $\overline{H_0}$, with $\overline{Z_0}$. In the tropics, the mean difference between $\overline{H_0}$ and $\overline{Z_0}$ is on the order of -600 m, with variability depending on seasonal, geographical, and climatic influences (Table 1, Figures 8-11).

4.2. Statistics and Climatology

In order to study the structure and variability of Z_0 , the following statistics are computed using 20 years of NCEP reanalysis data: individual monthly means, $\overline{Z_0}$; climatological monthly means, $\langle \overline{Z_0} \rangle$; monthly anomalies, $\overline{Z_0} - \langle \overline{Z_0} \rangle$; monthly standard deviations of instantaneous Z_0 values, s_0 ; and the standard deviations of the monthly means, S_0 . The instantaneous Z_0 field has a complex appearance, related to the structure of the temperature field, which is closely tied to the weather. Averaging over time yields smoother fields for $\overline{Z_0}$ and $\langle \overline{Z_0} \rangle$. The $\overline{Z_0}$ and $\langle \overline{Z_0} \rangle$ analysis (Figures 3 and 6) reveals that Z_0 is highest in the tropics (~4900 m), with a relatively flat, symmetric distribution around the equator. $\overline{Z_0}$ decreases rapidly poleward of 25°N or S. The s_0 and S_0 analyses (Figures 4 and 5) show that the lowest variabilities (~75-100 m), occur in the tropics. Variability increases poleward, peaking in mid-latitudes at about 400 m. Because the TRMM PR $\overline{H_0}$ data currently span only 13 months, the NCEP data can be used to estimate the interannual variability from the 20-year climatology.

The 1998 monthly anomalies (Figure 7) are almost exclusively positive values, indicating that 1998 is warmer than the 20-year climatology. In the tropics, in the first half of 1998, the anomalies are high in the eastern Pacific. As the year progresses, this feature diminishes gradually to low values in the second half of the year. High anomalies are seen more frequently, but on shorter time scales, in mid-latitudes. On a global scale, positive Z_0 anomalies are linked to increasing planetary temperatures. This is consistent with *Diaz and Graham* [1996], who found a strong link between observed changes in freezing level heights, the long-term (decadal-scale) increase in tropical sea-surface temperatures, and enhancement of the tropical hydrological cycle.

Zonal means $[\overline{Z_0}]$ of the 1979-1998 climatology exhibit a flat distribution of Z_0 in the tropics. Values decrease rapidly away from the tropics, with most rapid change

occurring across the mid-latitudes. Lowest values are found in higher latitudes, as would be expected. The zonal s_0 error bars indicate lower variability around the equator, with increasing variability toward the poles, independent of season or hemisphere.

4.3. Comparisons

Estimates of $\overline{H_0}$ from the TRMM PR data are compared with the 20-year NCEP climatology and 1998 monthly data. In the difference maps, missing data substantially hampers the analysis. Missing data occurs for two reasons: 1) NCEP data is flagged as missing when no freezing level is found (profile temperature is always $< 0^\circ \text{C}$) at any time during the averaging period, or 2) TRMM PR data is flagged as missing when no echoes meeting the criteria of the H_0 retrieval algorithm are identified. Additionally, since the PR is wholly dependent on the presence of rain to gather data, $\overline{H_0}$ is biased toward "rainy" conditions. Sampling error also affects the $\overline{H_0}$ field, as some grid boxes have few samples for the computation of $\overline{H_0}$ due to lack of rain during TRMM overpasses.

The 1998 mean-difference (Figure 8) maps are noisy but show that the difference between $\overline{H_0}$ and $\overline{Z_0}$ is nearly always positive. Averaging over the entire year helps to smooth the noise in the monthly raw difference maps. A notable feature is exposed in the yearly mean box plot (Figure 9). A pair of darker bands, one at 20°N and the other at 20°S , represent consistently higher differences than elsewhere over the Pacific, and are a reflection of the peaks in the zonal comparisons (Figure 11) that show up at 20°N and S in the winter hemisphere.

The differences found in this research differ from previous values in the literature. The values found here are higher than those in *Austin and Bemis* [1950] and *Stewart et al.* [1984]. *Austin and Bemis* [1950] found a mean difference between the

altitude of the 0° C isotherm and the bright band of about -300 m in various types of precipitation in Massachusetts, while *Stewart et al.* [1984] noted a difference of about -300 m in stratiform rain in California. However, the differences found in this research are lower than the values found in *Leary and Houze* [1979], who found a difference of -500 m to -900 m in GATE convection. Generally, values range from a minimum mean difference over the oceans of about -300 m to a maximum mean difference of up to around -900 m over continental areas, and in the latitude bands at 20°N and S.

In the zonal-mean difference comparisons (Figures 10 and 11), the similarity in shape of the two curves, $[\overline{Z}_0]$ and $[\overline{H}_0]$ is seen. Both $[\overline{Z}_0]$ and $[\overline{H}_0]$ decrease in magnitude through the year, with $[\overline{Z}_0]$ returning to its values from the positive anomalies in the first part of 1998. The changes in the $[\overline{Z}_0]$ and $[\overline{H}_0]$ curves are likely due to the strong El Nino of 1998. This anomalous event raised sea-surface temperatures (SSTs) over the Pacific Ocean significantly in the first half of the year, while the ensuing La Nina dramatically reduced SSTs in the eastern Pacific in the second half of the year. Due the strong link between SSTs and \overline{Z}_0 , these changes in SSTs shift the \overline{H}_0 (and \overline{Z}_0) fields higher (warm SSTs) and lower (cold SSTs).

It is difficult to make specific conclusions on a comparison with a one-year data set. However, it appears that the procedure developed by Shin for estimating the "freezing level" via the melting layer height is reasonable; it compares well to the NCEP freezing level climatology and the monthly-mean data. Evaluation of time series of difference data ($[\overline{H}_0] - [\overline{Z}_0]$, not shown) does not show any consistent trends during 1998.

REFERENCES

- Austin, P. M., and A. C. Bemis, A Quantitative Study of the "Bright Band" in Radar Precipitation Echoes, *Journal of Meteorology*, 7, 145-151, 1950.
- Cheng, C. C., and R. A. Houze, The Distribution of Convective and Mesoscale Precipitation in GATE Radar Echo Patterns, *Mon. Weather Rev.*, 107, 1370-1381, 1979.
- Chiu, L. S., G. R. North, D. A. Short, and A. McConnell, Rain Estimation from Satellites: Effect of Finite Field of View, *J. Geophys. Res.*, 95, 2177-2185, 1990.
- Diaz, H. F., and N. E. Graham, Recent Changes in Tropical Freezing Heights and the Role of Sea Surface Temperature, *Nature*, 383, 152-155, 1996.
- Houze, R. A., Stratiform Precipitation in Regions of Convection: A Meteorological Paradox?, *Bull. Amer. Meteor. Soc.*, 78, 2179-2196, 1997.
- Kalnay, E., M. Kanamitsu, R. Kistler, W. Collins, D. Deaven, L. Gandin, M. Iredell, S. Saha, G. White, J. Woollen, Y. Zhu, M. Chelliah, W. Ebisuzaki, W. Higgins, J. Janowiak, K. C. Mo, C. Ropelewski, J. Wang, A. Leetmaa, R. Reynolds, R. Jenne and D. Joseph, The NCEP/NCAR 40-Year Reanalysis Project, *Bull. Amer. Meteor. Soc.*, 77, 437-470, 1996.
- Kummerow, C., W. Barnes, T. Kozu, J. Shiue, and J. Simpson, The Tropical Rainfall Measuring Mission (TRMM) Sensor Package, *J. Atmos. and Oceanic Technol.*, 15, 809-817, 1998.
- Leary, C. A., and R. A. Houze, Melting and Evaporation of Hydrometeors in Precipitation from the Anvil Clouds of Deep Tropical Convection, *J. Atmos. Sci.*, 36, 669-679, 1979.
- Liu, G. and J. A. Curry, An Investigation of the Relationship between Emission and Scattering Signals in SSM/I Data, *J. Atmos. Sci.*, 55, 1628-1643, 1998.
- Rinehart, R. E., *Radar for Meteorologists*, 428 pp., Rinehart Publications, Grand Forks, N.D., 1997.
- Shin, K.-S., and G. R. North, Sampling Error Study for Rainfall Estimates by Satellite Using a Stochastic Model, paper presented at Tenth Conference On Probability and Statistics, Edmonton, Oct. 4-5, 1987.

- Shin, K.-S., P. E. Riba, and G. R. North, Estimation of Area Averaged Rainfall over Tropical Oceans from Microwave Radiometry: A Single Channel Approach, *J. Appl. Meteor.*, 29, 1031-1042, 1990.
- Simpson, J., G. R. North, and R. F. Adler, A Proposed Tropical Rainfall Measuring Mission (TRMM) Satellite, *Bull. Amer. Meteor. Soc.*, 69, 278-295, 1988.
- Stewart, R. E., J. D. Marwitz, and J. C. Pace, Characteristics through the Melting Layer of Stratiform Clouds, *J. Atmos. Sci.*, 41, 3227-3237, 1984.
- Tesmer, J. R. and T. T. Wilheit, An Improved Microwave Radiative Transfer Model for Tropical Oceanic Precipitation, *J. Atmos. Sci.*, 55, 1674-1688, 1998.
- Tokay, A., and D. A. Short, Evidence from Tropical Raindrop Spectra of the Origin of Rain from Stratiform versus Convective Clouds, *J. Appl. Meteor.* 35, 355-371, 1996.
- TRMM Science Data and Information System, *Interface Control Specification Between the Tropical Rainfall Measuring Mission Science Data and Information System (TSDIS) and the TSDIS Science User (TSU)*, Vol. 3, *File Specifications for TSDIS Products - Level 1*, Release 3.04, General Sciences Corporation, Greenbelt MD, 1997.
- Wilheit, T. T., A. T. C. Chang, M. S. V. Rao, E. B. Rodgers, and J. S. Theon, A Satellite Technique for Quantitatively Mapping Rainfall Rates over the Oceans, *J. Appl. Meteor.*, 16, 551-560, 1977.
- Wilheit, T. T., Some Comments on Passive Microwave Measurement of Rain. *Bull. Amer. Meteor. Soc.*, 67, 1226-1232, 1986.
- Willis, P. T., and A. J. Heymsfield, Structure of the Melting Layer in Mesoscale Convective System Stratiform Precipitation. *J. Atmos. Sci.*, 46, 2008-2025, 1989.
- Zipser, E. J., and M. A. Lemone, Cumulonimbus Vertical Velocity Events in GATE. Part II: Synthesis and Model Core Structure. *J. Atmos. Sci.*, 37, 2458-2469, 1980.